

NPS

①
N00123-89-G-0580

AD-A241 340



Propulsion Optimization for ABE,
an Autonomous Underwater Vehicle (AUV)

by

THOMAS JAMES WOODFORD
B.S. Electrical Engineering
University of Virginia (1983)

DTIC

Submitted in partial fulfillment of the
requirements for the degree of

MASTER OF SCIENCE IN OCEANOGRAPHIC ENGINEERING

at the

MASSACHUSETTS INSTITUTE OF TECHNOLOGY

and the

WOODS HOLE OCEANOGRAPHIC INSTITUTION

September 1991

© Thomas J. Woodford, 1991

The author hereby grants to MIT and WHOI permission to
reproduce and distribute copies of this thesis document in whole or
in part.

Signature of Author

Joint Program in Oceanographic Engineering
Massachusetts Institute of Technology
Woods Hole Oceanographic Institution
August 27, 1991

Certified by

Dr. Dana R. Yoerger
Associate Scientist
Woods Hole Oceanographic Institution
Thesis Supervisor

Accepted by

Dr. W. Kendall Melville, Chairman
Joint Committee for Oceanographic Engineering
Massachusetts Institute of Technology
Woods Hole Oceanographic Institution



91-12497



91 10 4 000

Propulsion Optimization for ABE, an Autonomous Underwater Vehicle (AUV)

by

THOMAS JAMES WOODFORD

Submitted to the Massachusetts Institute of Technology/
Woods Hole Oceanographic Institution
Joint Program in Oceanographic Engineering
on August 27, 1991 in partial fulfillment of the
requirements for the degree of

MASTER OF SCIENCE IN OCEANOGRAPHIC ENGINEERING

ABSTRACT

2) The oceanographic community is moving towards unmanned autonomous vehicles to gather data and monitor scientific sites. The mission duration of these vehicles is dependent primarily on the power consumption of the propulsion system, the control system and the sensor packages.

A customized propulsion thruster is designed. This includes a specialized propeller tailored to ABE and a matched motor and transmission. A non-linear lumped parameter model of the thruster is developed and experimentally verified. The model is used to predict thruster performance and compare the design thruster with other variants of propeller and motor/transmission combinations.

The results showed that there is a trade-off between rapid dynamic response and power conservation. For the typical ABE trajectory, the designed thruster provides good dynamic response and the lowest power consumption of all the modelled thruster units.

Thesis Supervisor: Dr. Dana R. Yoerger
Associate Scientist
Woods Hole Oceanographic Institution

Acquisition	✓
Dist. Special	
Dist. Tel	
Dist. Int. of	
Dist. Information	
Spec. Form 50	
Distribution	
Acquisition of	
Acquisition of	
Dist	Special
A-1	

Acknowledgements

The completion of this thesis was made possible by the support and encouragement of my friends and colleagues at the Deep Submergence Laboratory, who provided advice, help and a constant reminder of reality.

Through the many trials and tribulations of preparing a thesis (including hurricane Bob which wreaked havoc on the Woods Hole Oceanographic Institution on 19 August 1991 and left the area without electrical power for nearly a week) I am especially grateful to my wife Elizabeth. She stood by and provided constructive criticism, proof reading service, and kept her good humor in spite of being forced to live the life of a gypsy as we moved between sources of power for my computer. For this invaluable service, I dedicate this paper to her.

The United States Navy is gratefully acknowledged for the graduate education opportunity provided. This research was also supported by the National Science Foundation, grant number OCE 8820227.

Author's Biographical Note

LT Thomas J. Woodford, USN, completed his undergraduate studies at the University of Virginia, receiving a Bachelor of Science in Electrical Engineering and was commissioned in the U.S. Navy in 1983. He completed nuclear propulsion and Surface Warfare training in 1984 and was assigned to the USS TRUXTUN (CGN-35). On TRUXTUN he served as Damage Control Assistant and Electrical Officer. He served as Shift Engineer for the D1G prototype at the Nuclear Power Training Unit, Ballston Spa, New York prior to his current assignment in the Massachusetts Institute of Technology/ Woods Hole Oceanographic Institution Joint Program in Oceanographic Engineering.

LT Woodford's next assignment, following completion of his graduate studies, will be at the Surface Warfare Officer School's Department Head Course in Newport, Rhode Island. Following this school, he will be assigned as a Department Head aboard a small combatant vessel of the U. S. Navy.

Contents

Chapter 1.	Introduction	
1.1	Motivation.....	11
1.2	Research Objectives.....	13
1.3	Outline of Thesis.....	14
Chapter 2.	The Propeller and Duct	
2.1	Introduction to Propeller Design.....	15
2.2	ABE Vehicle Constraints.....	16
2.3	Optimum Efficiency.....	19
2.4	MIT-PUL Parametric Study.....	21
2.5	MIT-PBD10 Blade Shaping.....	25
2.6	The Duct.....	30
2.7	Experimental Propeller.....	33
Chapter 3.	The Motor and Gearbox	
3.1	ABE Vehicle Constraints.....	35
3.2	DC Brushless Motors.....	37
3.3	The Fill Fluid and Windage.....	39
3.4	The Gearbox.....	40
3.5	Matching the Motor with the Propeller.....	41
3.6	Sensitivity of the Analysis.....	45
Chapter 4.	The Lumped Parameter Model of the Propulsor	
4.1	Introduction.....	46
4.2	Description of the Thruster Unit.....	46

4.3	The Complete Model.....	59
4.4	Simulation.....	62
4.5	Summary.....	63
 Chapter 5. Experimental Verification		
5.1	Experimental Setup.....	64
5.2	Steady State Response.....	66
5.3	Step Response.....	66
5.4	Sinusoidal Response.....	67
5.5	Summary.....	73
 Chapter 6. Steady State Performance Comparison of Several Thruster Units.		
6.1	Introduction.....	75
6.2	ABE Thruster and the Other Thrusters.....	76
6.3	Steady State Comparison.....	80
6.4	Summary.....	84
 Chapter 7. Balancing Dynamics and Efficiency		
7.1	Introduction.....	85
7.2	Dynamic Comparison.....	88
7.3	An Open Loop Force Controller.....	89
7.4	Summary.....	97
 Chapter 8. Summary, Conclusions, and Recommendations.....		
		99

Figures

1.1	The Basic ABE Design.....	12
1.2	The Typical ABE Mission Profile.....	13
2.1	Kramer Ideal Propeller Efficiency.....	20
2.2	The Assumed Inflow Velocity Field.....	22
2.3	Efficiency versus Required Thrust.....	24
2.4	Propeller Chord Distribution.....	27
2.5	Propeller Camber Distribution.....	28
2.6	Propeller Thickness Distribution.....	28
2.7	Propeller Pitch Distribution.....	29
2.8	Propeller Planar Blade Shape, No Skew.....	29
2.9	Propeller Planar Blade Shape, Slight Skew.....	30
2.10	5% Propulsive Duct.....	32
2.11	Duct Cross-sectional Shape.....	32
2.12	Experimental Propeller Chord Distribution.....	33
2.13	Experimental Propeller Pitch Distribution.....	34
2.14	Experimental Propeller Planar Blade Shape.....	34
3.1	Motor Schematic.....	38
3.2	Thruster System Block Diagram.....	41
3.3	System Efficiencies.....	44
3.4	Total System Efficiency.....	44
4.1	Schematic Representation of the Thruster Unit...	47

4.2	Schematic Representation of the Propeller and Duct Assembly.....	48
4.3	Bond Graph for the Propeller and Duct Assembly..	54
4.4	Gearbox Schematic Diagram.....	55
4.5	Bond Graph for the Gearbox.....	56
4.6	The Motor Assembly.....	57
4.7	The Motor Bond Graph.....	58
4.8	The Complete Model Bond Graph.....	59
4.9	The Complete Model Block Diagram.....	61
4.10	The Simplified Block Diagram.....	62
5.1	The Experimental Test Stand.....	65
5.2	Model Step Response.....	66
5.3	Actual Thruster Step Response.....	67
5.4	Actual and Model Sinusoid Response, $T=10$	68
5.5	Actual and Model Sinusoid Response, $T=5$	69
5.6	Actual and Model Sinusoid Response, $T=2.5$	70
5.7	Actual and Model Sinusoid Response, $T=1.25$	71
5.8	Actual and Model Sinusoid Response, $T=0.625$	72
6.1	The Jason Propeller Response.....	78
6.2	The 18" Diameter, 6" Pitch Airplane Propeller Response.....	79
6.3	The 18" Diameter, 8" Pitch Airplane Propeller Response.....	80
6.4	The Experimental Propeller Response.....	81
6.5	Propeller Comparison, Torque Mode, MFM Motor....	83
6.6	Propeller Comparison, Velocity Mode, MFM Motor..	83

7.1	Simulation Tracks.....	87
7.2	Power Consumption.....	95
7.3	Experimental Thruster Track #2, Velocity Response.....	96
7.4	M88 Thruster Track #2, Velocity Response.....	96
7.5	Thruster Hover Response.....	97

Chapter 1

Introduction

1.1 Motivation

The Woods Hole Oceanographic Institution (WHOI) is currently developing an autonomous underwater vehicle (AUV) for scientific survey of the ocean floor. This vehicle has been designated **ABE**, for the **A**utonomous **B**enthic **E**xplorer.

As the oceanographic community explores the ocean floor, the reliance on manned submarines to maintain ongoing experiments has become restrictive. **ALVIN**, WHOI's manned deep submersible, is unable to undertake new research, due to an exhaustive schedule maintaining experiments that are already in progress. **ABE** is being developed in order to free up assets such as **ALVIN** and **JASON**, WHOI's unmanned submersible, by performing routine data collection and surveying at remote ocean bottom scientific sites. Additionally, since **ABE** can operate without a nearby surface ship operating as a tender/control ship, **ABE** will also free up valuable research vessel time. In these respects, **ABE** will complement the existing capabilities of tethered and manned submersibles.

ABE will be a long endurance vehicle with a typical deployment of one year in length. This compares to an on-station endurance of eight hours for a manned research submersible (ALVIN) and around a month for tethered robots (JASON). During the deployment, ABE will observe a relatively small area (on the order of square kilometers) of the ocean floor at frequent intervals. Figures 1.1 and 1.2 show the preliminary ABE configuration and a typical mission profile.

During a mission, ABE will remain in a semi-dormant state for the majority of the time. At a predetermined interval or in response to a trigger event, ABE will wake, and perform a photographic survey along a preprogrammed flight path. Upon completion of the survey, ABE will return to its mooring, power down and wait for the next survey time.

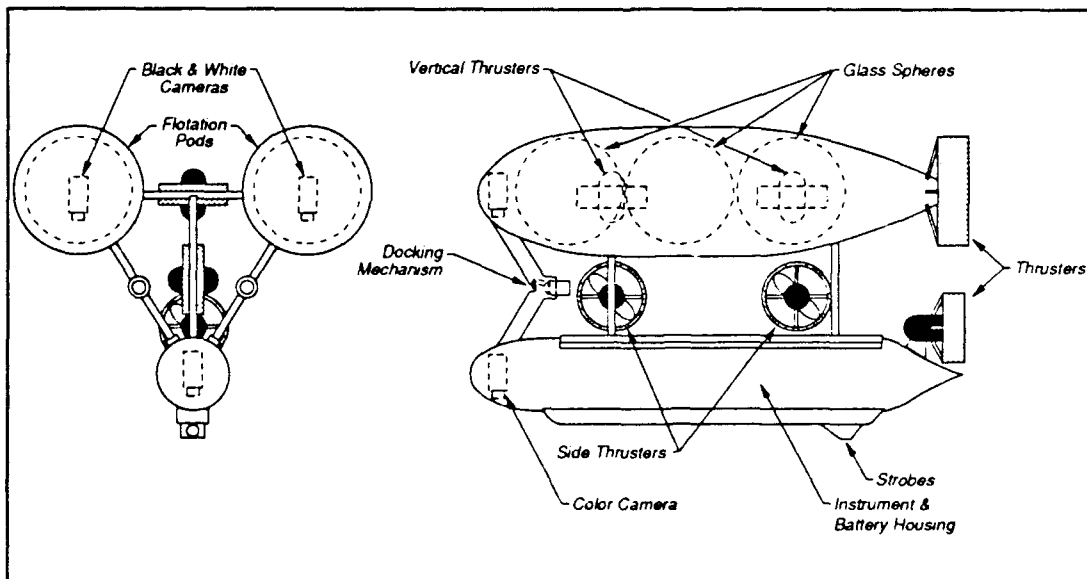


Figure 1.1 The Basic ABE Design.[1]

In order for ABE to have sufficient battery power for a one year mission, careful attention must be paid to developing a highly efficient propulsion system. This research is motivated by the need to develop this propulsion system.

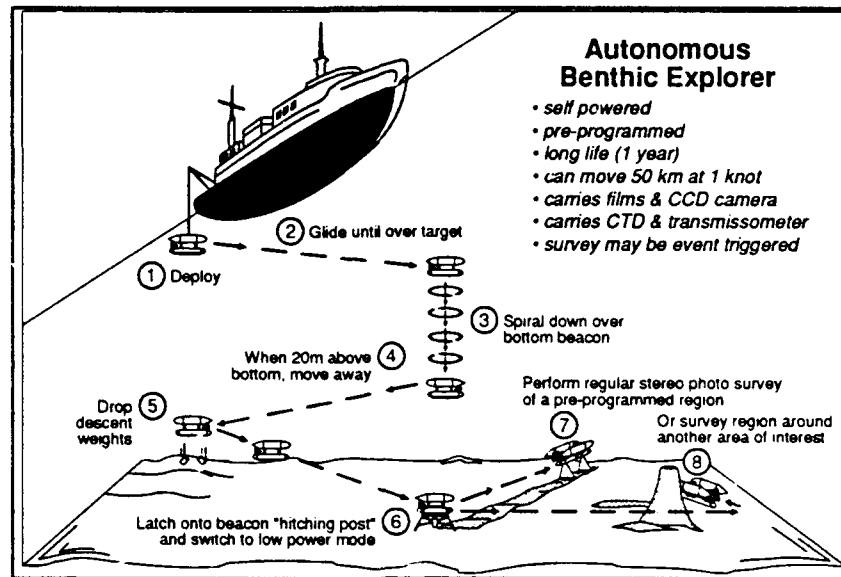


Figure 1.2 The Typical ABE mission profile will consist of four phases: Descent (1-6), Sleep (6), Survey (7-8), and Ascent. [1]

1.2 Research Objectives

There are two major components of a AUV propulsion system. The first is the mechanical/hydrodynamic system commonly referred to as a thruster or propulsor. The thruster consists of an electric motor, a transmission and a propeller/duct. The second component is the electronics and the algorithm used to control the mechanical system.

The thruster must be optimized for the specific vehicle. This involves designing a specialized propeller and duct assembly then matching a suitable motor and gearbox to take advantage of the motor's high speed efficiency and the propeller's low speed efficiency. This is done to maximize the conversion of electrical energy to thrust.

The control system must then be designed to provide the best possible dynamic response, while taking advantage of the mechanical system's most efficient operating conditions.

The objective of this research is to develop a propulsion system that provides good dynamic response while maintaining the high efficiency needed by ABE to perform its mission.

1.3 Outline of Thesis

Chapter 2 presents the design of an efficient propeller for the ABE vehicle. Chapter 3 examines the selection of a motor and gearbox matched to the ABE propeller. In Chapter 4, a lumped parameter model of the thruster is developed. Chapter 5 contains the experimental verification of the model.

Chapter 6 compares the steady state performance of the designed ABE thruster with other thruster units. Chapter 7 examines the trade-offs that must be made between power efficiency and beneficial dynamics. Chapter 8 summarizes the results of the thesis and provides recommendations for further research.

Chapter 2

The Propeller and Duct

The goal of this chapter is to develop a propeller and duct combination for ABE that optimize the power conversion of the thruster.

2.1 Introduction to Propeller Design

The propeller design presented here is based on the Massachusetts Institute of Technology's (MIT's) propeller development software. This software uses Lifting Line Theory and optimum circulation to solve the complex hydrodynamics of a marine propeller. [2]

The process used to design the propeller for ABE is as follows:

1. Calculate the drag of the tentative ABE vehicle at the desired operating velocity.
2. Determine the thrust required.
3. Determine the physical constraints of the vehicle that effect propeller size.
4. Estimate the wake field near the propeller.

5. Perform a parametric study using MIT's Propeller Lifting Line program (MIT-PLL). Minimize Power and torque for a given thrust.

6. Use MIT's Propeller Blade Design program (MIT-PBD10) to calculate the blade shape from MIT-PLL's optimum output.

2.2 ABE Vehicle Constraints

2.2.1 ABE Physical Considerations

The ABE vehicle consists of two buoyancy pods supporting a single instrument cylinder underneath. The buoyancy pods are twenty one inch diameter series 58 bodies, and the instrument cylinder is a twelve inch diameter streamline cylinder. All three bodies are seven feet long and they are connected by a series of struts. There are seven thruster/propulsor units on ABE. Three are main propulsors mounted at the stern of each cylinder. The remaining four are thrusters for attitude and depth control. Two of these last four thrusters are mounted vertically, and the other two are mounted athwartships. ABE is designed to have a cruising speed of one knot, and a minimum sprint capability of two knots. The power budget allows 100 watts for normal propulsion with a peak of 200 watts available. The propulsors

are limited to a diameter of eighteen inches by the space available on ABE.

2.2.2 Vehicle Drag

The buoyancy pods are made up of twenty-one inch, series 58, streamlined shapes. Each pod will have a surface area of 28.1 ft². The drag on this type of body for relatively slow speeds is primarily due to friction on the surface. The drag can be calculated from the following equation:

$$Drag = \frac{1}{2} \rho U^2 C_D S \quad (2.1)$$

Where the drag coefficient, C_D , is approximately equal to the flat plate frictional drag coefficient, C_F . For ABE at one knot in seawater, the Reynold's Number is $\approx 6 \times 10^5$ and the corresponding C_F is ≤ 0.007 . [3] S is the wetted surface area, U is the velocity through the water, and ρ is the density of the seawater. Using this equation, the drag of each of the buoyancy pods at one knot is 0.56 lbf. The cylindrical instrument case will be fitted with streamlined nose and tail cones and equation (2.1) holds for this case as well. The drag for the twelve inch diameter instrument case at one knot is 0.44 lbf. The combined drag of the three main body sections of ABE is 1.6 lbf.

Attention must be paid to the struts connecting the body sections. Careful design of these structures can reduce vehicle drag significantly. If it is assumed that the struts are well designed and have a streamlined cross-section, then equation 2.1 above can be used to calculate the drag. The term S is now equal to the entire wetted surface of the strut (top and bottom surfaces). Assuming nine feet of struts with one inch maximum thickness and five inches width, the calculated drag is ≈ 0.15 lbf.

However, if the struts are poorly designed the drag increases by an order of magnitude. Assuming a 1-inch circular cross-section, the drag is now calculated by:

$$Drag_{STRUT} = \frac{1}{2} \rho U^2 d C_d \quad (2.2)$$

Where the drag coefficient, $C_d \approx 1.0$, for laminar flow and d is the diameter of the strut. For nine feet of circular struts the drag is approximately 2.25 lbf.

For ABE, the struts are assumed to be made up of streamlined shapes for two-thirds of the total length and bluff sections for the remaining length. The bluff sections account for joints, fouling, and imperfections in the strut sections. Using this distribution the drag due to the struts is 0.8 lbf at 1 knot.

A large portion of the drag will come from the attitude control thrusters. The attitude control thrusters are

comprised of four thrusters mounted perpendicular to the flow streamlines when ABE is traveling in the forward direction. These thrusters will be used to make minor corrections to the vehicle's depth and heading. These thrusters will be ducted to prevent fouling and impact damage. Each unit will have a 3 inch diameter, streamlined motor case and a 3 inch by 18 inch duct that will be streamlined for forward motion. Using the above equations, each thruster will have a drag of 0.2 lbf.

The total vehicle drag for a forward speed of 1 knot is 3.2 lbf. For the purposes of propeller design, each thruster will be designed to give 3 lbf at 1 knot. This allows ABE to maintain a full speed capability in the event of the failure of one of the three main propulsion thrusters. Additionally, ABE will have an excess propulsive force available during normal cruising conditions.

2.3 Optimum Efficiency

Using the thrust of 3 lbf determined from the drag, the vehicle's speed of one knot, an estimated shaft speed of 100 rpm, and the 1.5 foot propeller diameter, the ideal efficiency can be determined from the Kramer diagram, Figure 2.1 [2]. The entering arguments for the diagram are λ (a form of the ship advance coefficient, J_s) and C_T , the thrust coefficient.

For ABE these coefficients are:

$$\lambda = \frac{J_s}{\pi} = \frac{V_s}{\pi d} = \frac{1.6878 \frac{ft}{sec}}{\pi (100 rpm) (\frac{1}{60} \frac{min}{sec}) (1.5 ft)} = 0.22 \quad (2.3)$$

$$C_T = \frac{T}{\frac{1}{2} \rho \pi V_s^2 R^2} = \frac{31 bf}{\frac{1}{2} \pi (1.9905 \frac{lb f s^2}{ft^4}) (1.6878 \frac{ft}{s})^2 (.75 ft)^2} = 0.60$$

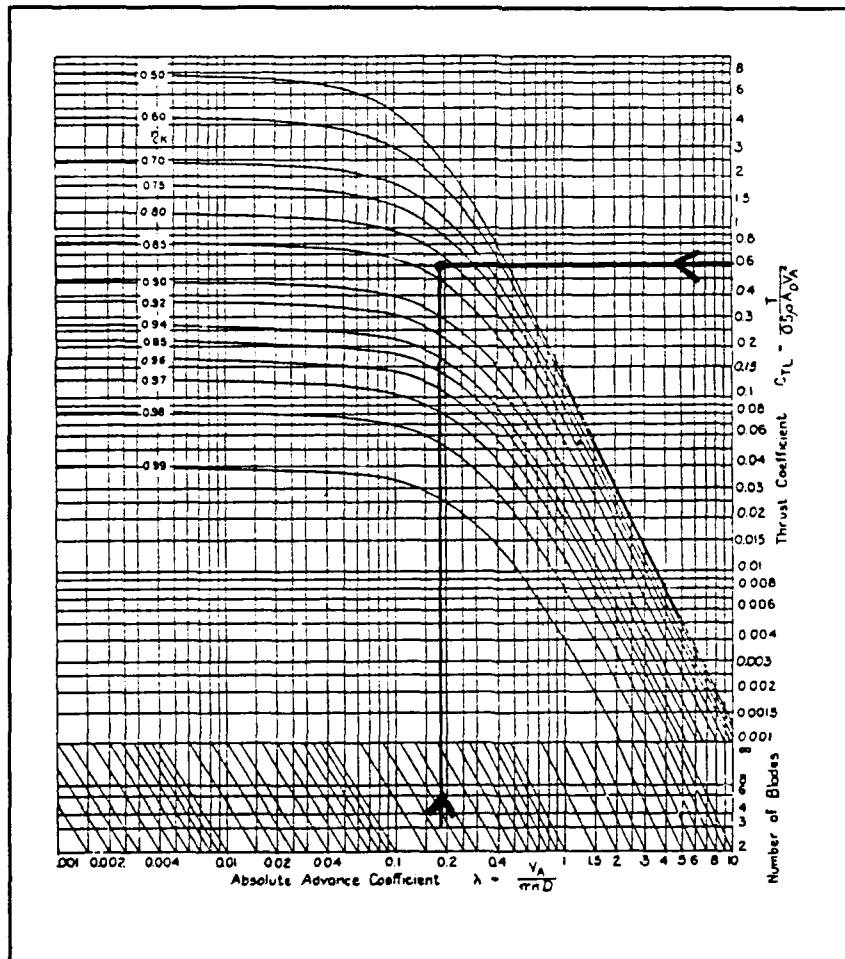


Figure 2.1 Kramer Ideal Propeller Efficiency [2]

The ideal efficiency for a three blade propeller operating under these conditions is $\eta_i \approx 83\%$. [2] This represents the maximum efficiency possible, neglecting viscous forces.

2.4 A Parametric Study using MIT-PLL

Using the information already discussed, we are almost ready to begin using MIT-PLL to start developing some chord and thickness distributions for the ABE propeller blade. In order to enter MIT-PLL, initial chord and thickness distributions must be assumed and a inflow velocity field needs to be determined.

The initial chord and thickness distribution were assumed to be linear. At the hub, the chord is 2 inches, the thickness is $\frac{1}{4}$ inch. At the blade tip, the chord is $\frac{1}{4}$ inch with a tenth of an inch thickness.

For an accurate inflow field to be determined, extensive model testing must be performed. Since this type of testing is beyond the scope of this paper, a simple inflow field is assumed. This field is shown in Figure 2.2.

With this information, a parametric study of several potential propellers was conducted. The parameters used in this study are: (1) Number of Blades, (2) RPM, and (3) Blade Shape (in a qualitative sense). The goal is to find the maximum efficiency and the minimum power required to generate

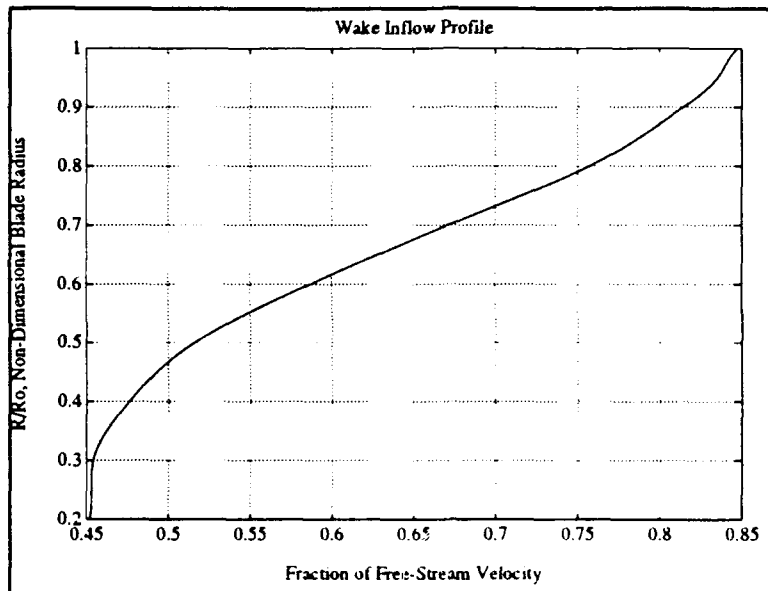


Figure 2.2 The assumed inflow velocity field

the required 3 lbf thrust, with an acceptable blade shape.

The first step is to determine the number of blades for the propeller. To do this, the required thrust was varied from the 3 lbf value calculated above. This determined two things: 1) How dependent efficiency calculations are on thrust, and 2) how dependent these calculations are on the number of blades. Table 2.1 shows the results of these runs. For each run, the optimum RPM was determined, the effective wake recalculated, circulation optimized and chord lengths optimized. The output was run through the cycle until horsepower, torque and efficiency remained constant. Figure 2.3 . shows the plot of efficiency versus thrust for $V_s=1$ knot and various numbers of blades. The figure shows that the number of blades has little effect on the efficiency over ABE's expected operating range.

Thrust→	0.5	1.0	2.0	3.0	4.0	5.0	8.0	10.0
Bld: 3	lbf	lbf	lbf	lbf	lbf	lbf	lbf	lbf
HP	.001	.003	.006	.010	.014	.018	.033	.044
Torque	.14	.23	.39	.54	.68	.82	1.22	1.48
RPM	45.5	58.7	77.9	92.8	105	115	142	157
η	.875	.819	.749	.702	.666	.637	.573	.542
Blades: 4								
HP	.001	.003	.006	.009	.014	.018	.033	.044
Torque	.15	.26	.43	.60	.75	.91	1.35	1.63
RPM	41.3	53.1	70.1	83.1	94.4	104	128	141
η	.875	.820	.751	.704	.668	.639	.576	.544
Blades: 5								
HP	.001	.003	.006	.009	.014	.018	.033	.044
Torque	.16	.28	.47	.65	.81	.97	1.44	1.75
RPM	38.9	48.2	65.2	77.2	87.7	96.9	119	131
η	.872	.818	.75	.704	.669	.640	.576	.545

Table 2.1 (No Tunnel Used in Calculations)

Over the range of thrust from 1 to 6 lbf, the three, four and five blade propellers show only a slight variation from each other. This difference can be considered statistically insignificant. The three, four and five blade propellers were used in the next stage of development. All propellers have comparable results.

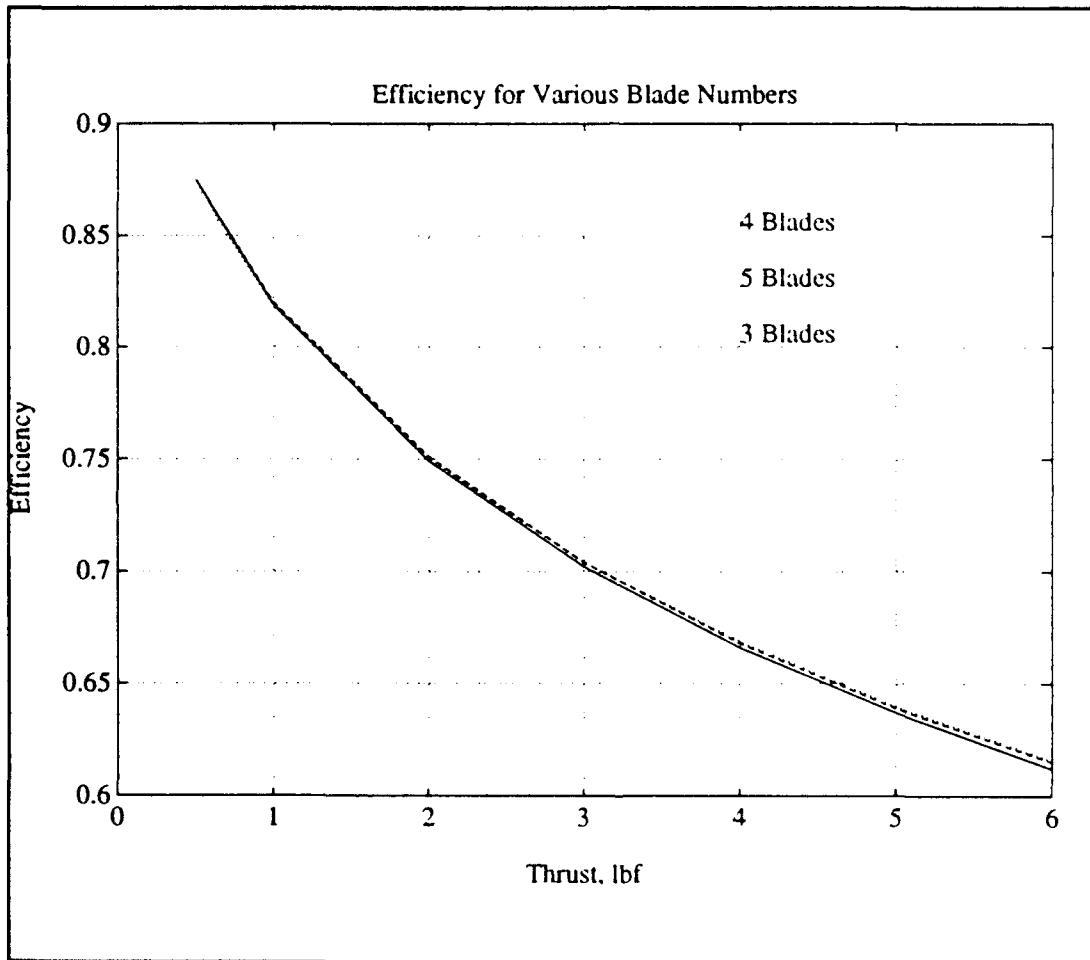


Figure 2.3 Efficiency, η versus required Thrust.

The evolution of the final blade took many iterations. The first 3-blade propeller had a predicted efficiency of $\approx 70\%$. (This was calculated without a tunnel around the

propeller.) The resulting chord distribution had an extremely narrow blade with a very sharp tip. This blade was not physically suited for use in the marine environment. Any fouling or impact with an obstruction (eg. fish) would have destroyed the blade.

Several chord distributions were used. By taking the output of one run, the planer blade shape was plotted (based on the chord distribution). From this plot, a new, more rugged chord distribution was developed. This chord distribution was used for the next MIT-PLL run as the initial blade input. For each run of MIT-PLL, the thrust (3 lbf), the diameter (1.5 ft) and the inflow velocity field were held constant. The RPM, circulation, and chord lengths were optimized. After several iterations, a final 3-blade propeller with a 66.1% efficiency and a 4-blade propeller with a 66.4% efficiency were chosen. These propellers showed the highest efficiency, with durable blade dimensions.

The three blade propeller is presented since a commercially available propeller similar to the designed propeller was readily obtained. The commercial propeller is presented in section 2.7 .

2.5 MIT-PBD10, Blade Shaping

After using MIT-PLL to determine the desired circulation, chord and thickness distributions, the actual blade shape and

camber that will develop the desired circulation must be calculated. The code used for this is MIT's Propeller Blade Design program, PBD10. To enter MIT-PBD10, a rake and skew of the blade is required in addition to the MIT-PLL output. Since rake has negligible effects and serves no purpose for the ABE vehicle, no rake is used. The primary purpose of skew is to balance (by phase shift) unsteady forces on the propeller. Since the forces on ABE are small and the speeds of operation are low, the unsteady forces are neglected and a small amount of skew (8° at the tip) was added to aid in obstruction shedding.

The recommended default values for MIT-PBD10 were used initially. These values determine the nature and extent of the wake field. The two dimensional blade cross-section shape was chosen as a NACA $a=0.8$ mean line. Slight modifications were made to the extent and contraction of the wake field in order for PBD10 to run smoothly in this particular case. The PBD10 output for K_T , K_Q and the induced velocities are similar to what was described by PLL. Figures 2.4 through 2.7 show the resulting blade shape determined by the above process. Figures 2.8 and 2.9 show a planer view of the blade, with and without skew.

The summary of the propeller designed is:

Number of Blades: $Z=3$

Hub Radius: $R_H=1.8"$

Tip Radius: $R_o=8.4"$

Duct OD: $D=18"$

ID: $d=17"$

Optimum RPM: $N=94.5$

@1 knot & 3 lbf

Horsepower: $P=.008$

Torque: $\tau=0.46 \text{ ft-lbf}$

Efficiency: $\eta=0.661$

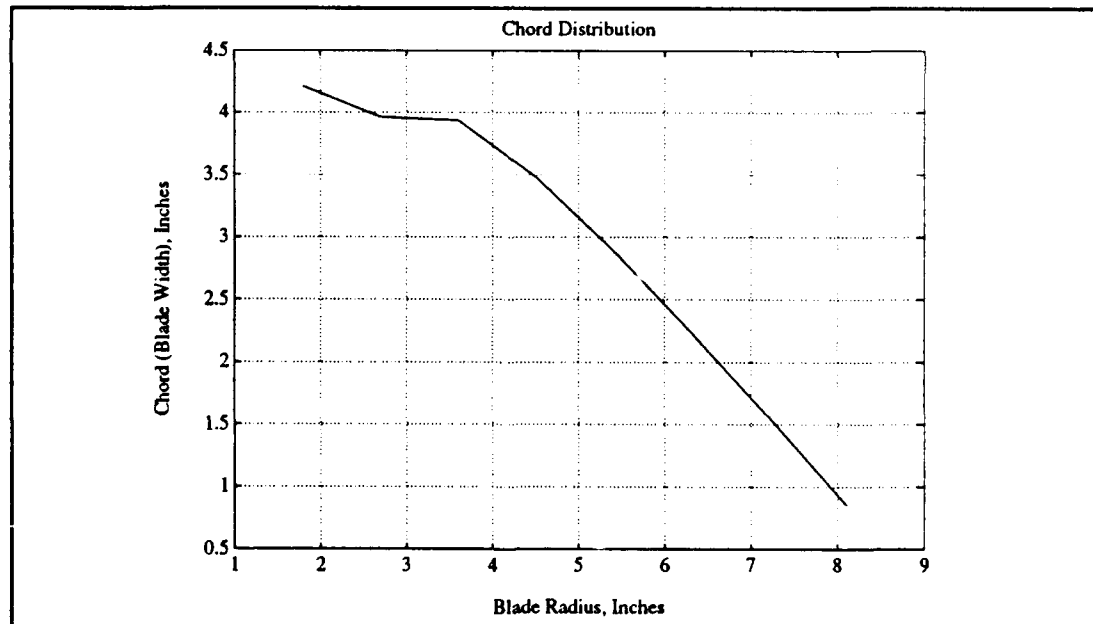


Figure 2.4 Chord Distribution

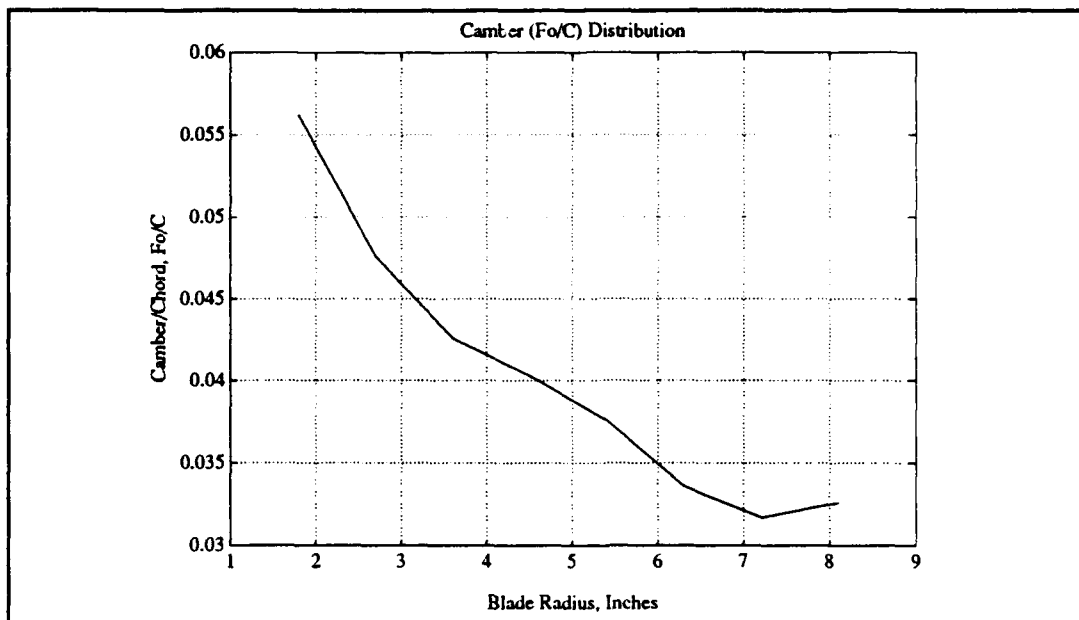


Figure 2.5 Camber Distribution

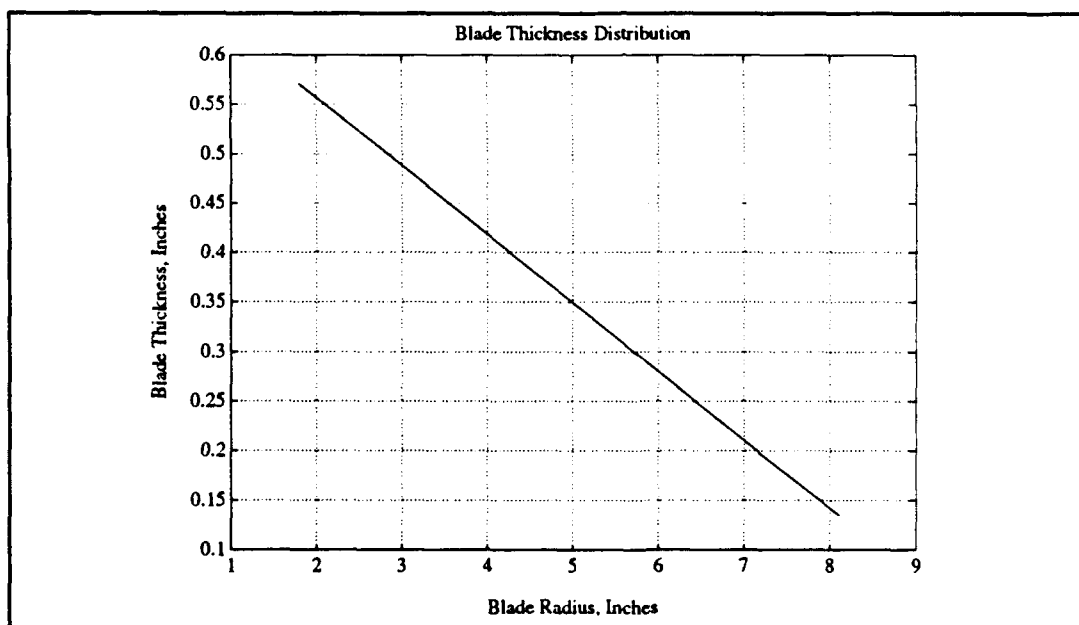


Figure 2.6 Thickness Distribution

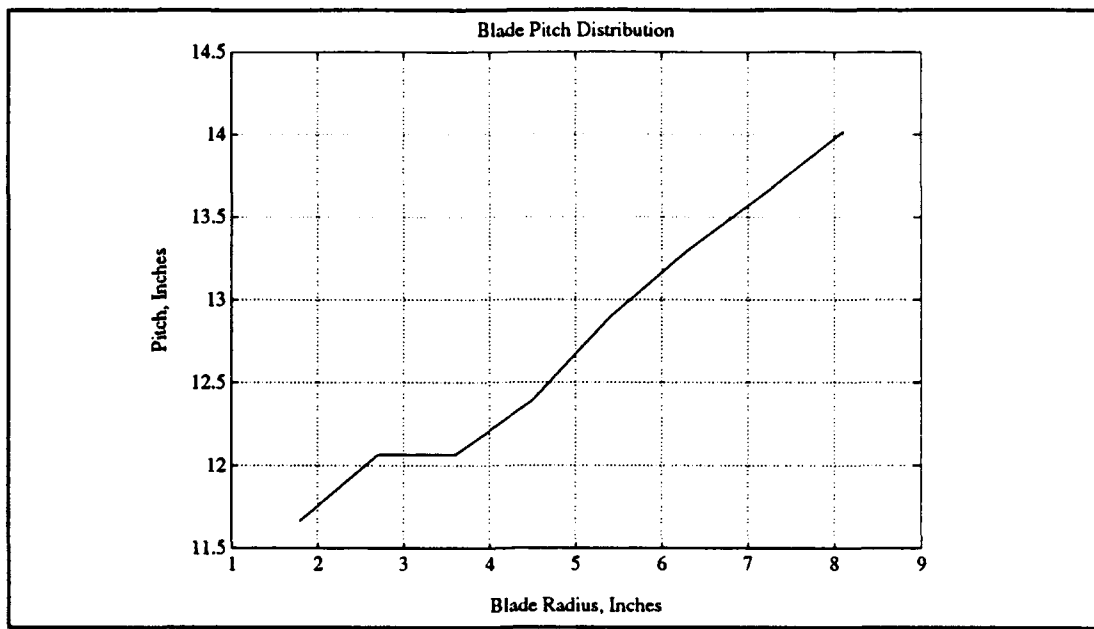


Figure 2.7 Pitch Distribution

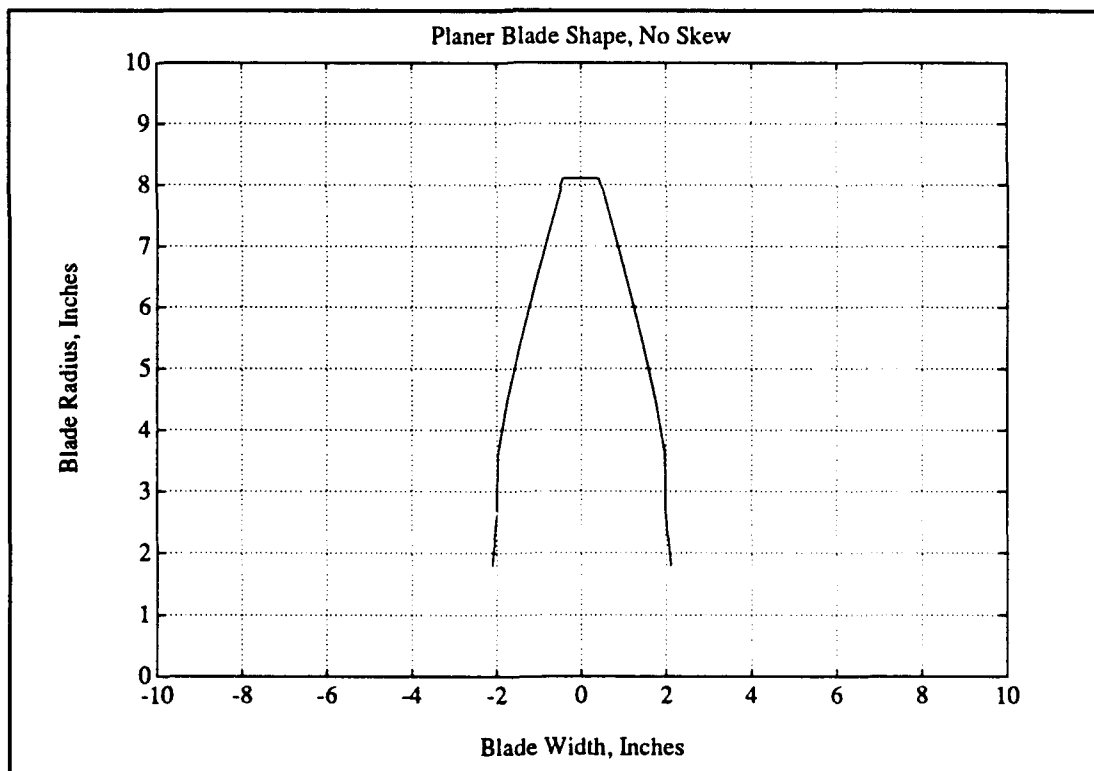


Figure 2.8 Planer Blade Shape, No Skew.

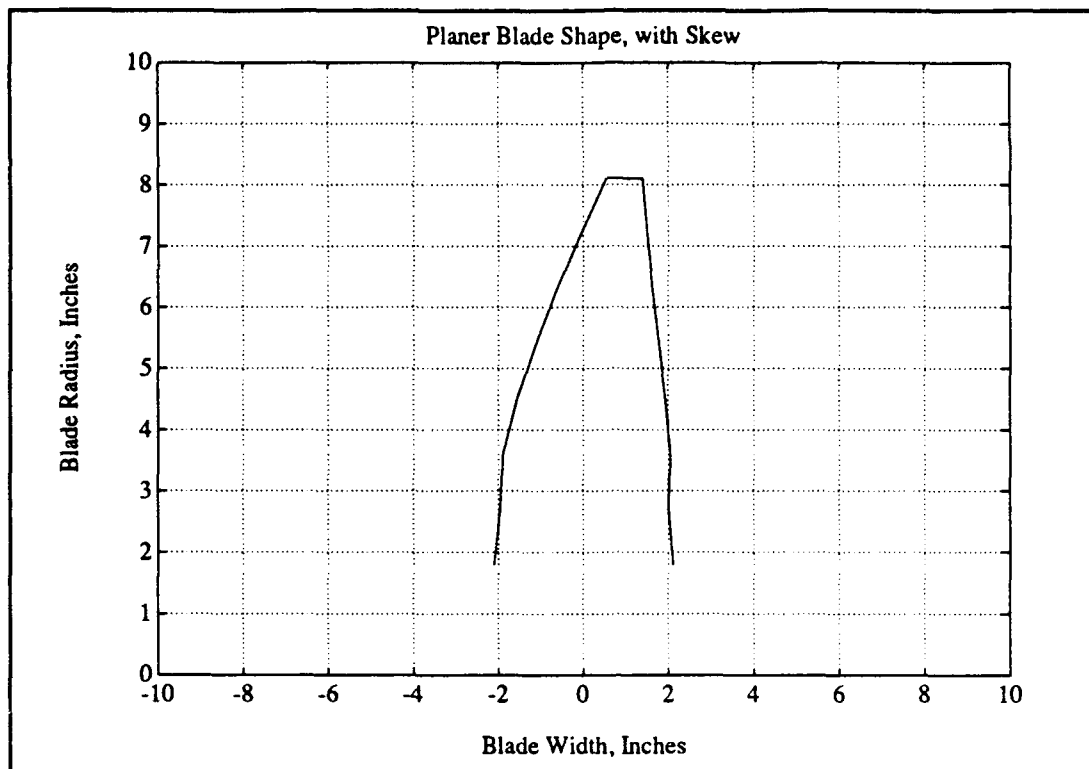


Figure 2.9 Planer Blade Shape, Light Skew.

2.6 The Duct

The next step in the ABE propulsor development is to design the duct. The primary purpose for the ducts on ABE is to prevent fouling of the propellers and the shafts during prolonged deployments. The goal is to design a low drag duct that has a minimal effect on the vehicle's hydrodynamics and propulsion efficiency. The MIT-PLL program traces the neutral streamlines at the tip of the propeller. If a duct is placed along these streamlines, the duct will have no effect on the propeller. If a slight angle of attack is placed on the duct, lift can be achieved on the duct section. This lift, when

summed around the entire duct, becomes a propulsive force (as opposed to drag). Using MIT-PLL, a duct with a slight propulsive force was designed. The neutral nose-tail angle of attack is 4.4 degrees. The angle of attack for 5% duct propulsion is 3.8 degrees. The cross-sectional shape for the duct is the NACA 0008 Basic thickness form. [4] Figures 2.10 and 2.11 show this duct.

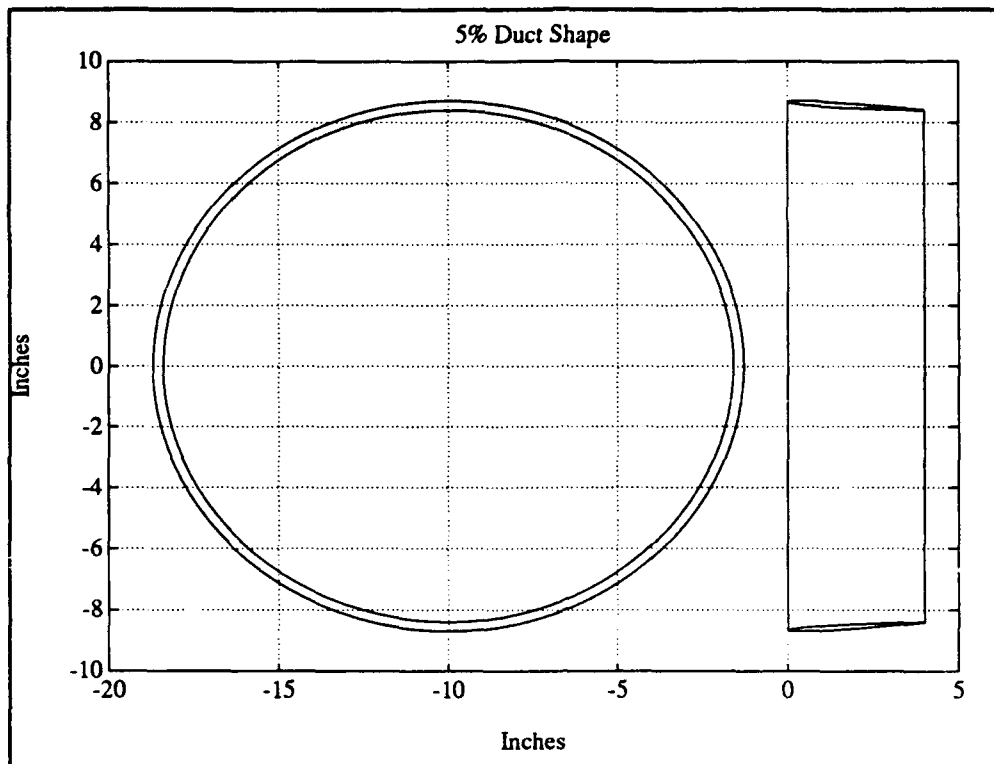


Figure 2.10 5% Propulsive Duct

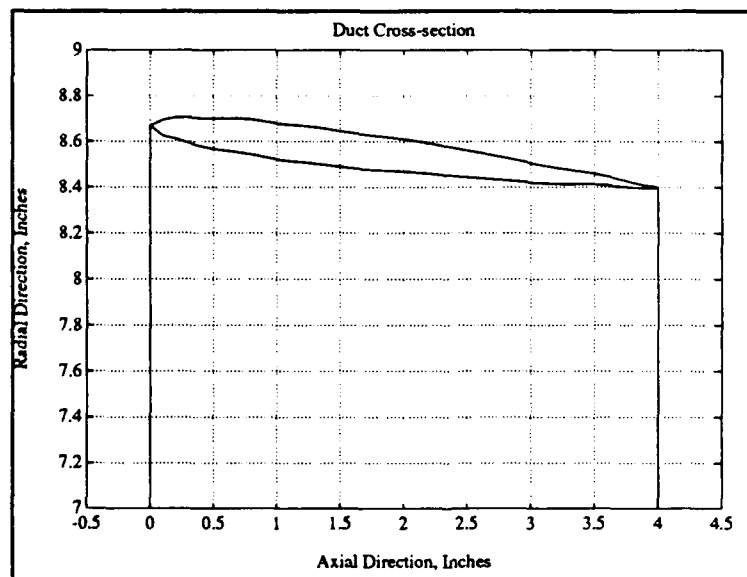


Figure 2.11 Duct Cross-Sectional Shape

2.7 The Experimental Propeller

The test propeller used in collecting data was a Michigan Wheel 18-inch diameter, 16-inch pitch, Sailer [™], 3-Blade propeller. This propeller was chosen because it most closely matches the chord and pitch distribution of the designed propeller. Figures 2.12 through 2.14 describe this propeller.

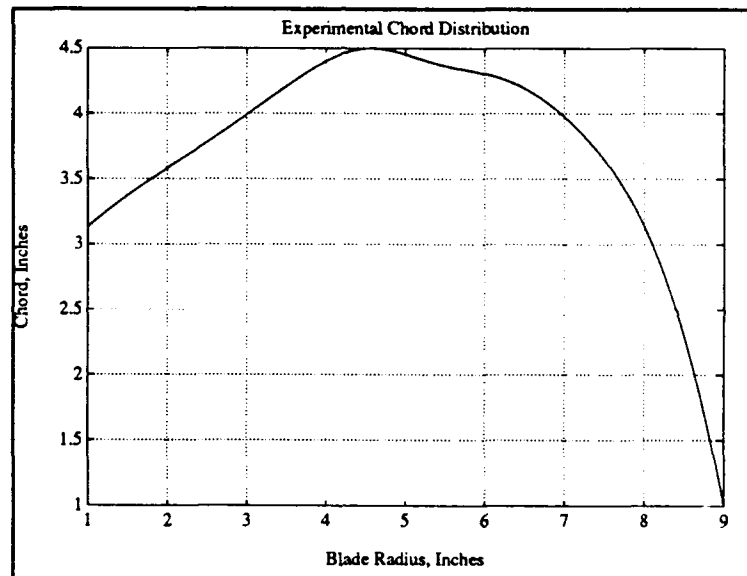


Figure 2.12 Experimental Propeller Chord Distribution

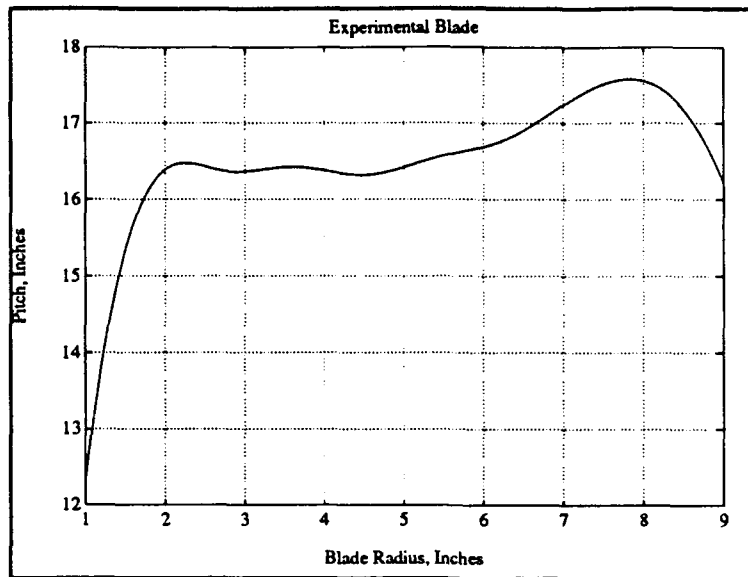


Figure 2.13 Experimental Propeller Pitch Distribution

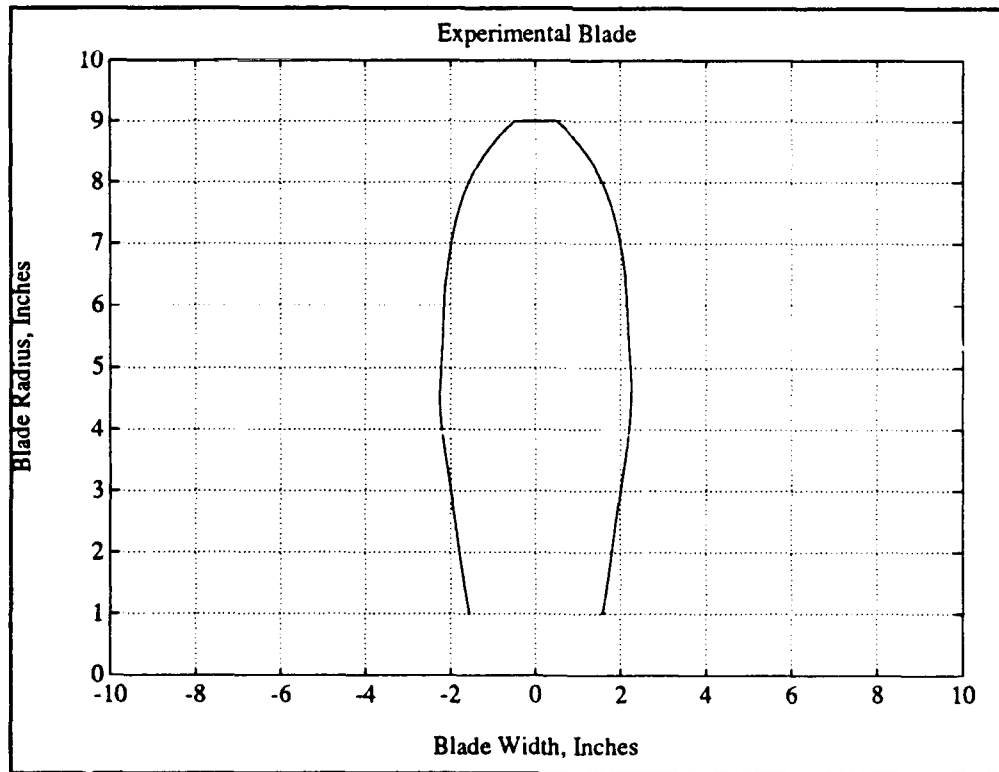


Figure 2.14 Experimental Propeller Planer Blade Shape

Chapter 3

The Motor and Gearbox

3.1 ABE Vehicle Constraints

There are several serious constraints placed on the mechanical design of the motor and transmission by ABE's mission environment. The two primary considerations are the ambient pressure of the ocean bottom and the limited supply of electrical power provided by onboard batteries.

In order to survive the extreme pressure (10,000 psi), the motor assembly must either be pressure tolerant or isolated from the pressure. In order to isolate the motor, a heavy pressure vessel must be constructed and the motor sealed inside. There must be a shaft seal around the output shaft. This seal must be leak proof at an extremely large differential pressure. Such a seal is expensive and produces a large added load on the motor. This load reduces system efficiency in a dramatic way. Pressure tolerant motors also require shaft seals. However, since the internal pressure of the motor casing is maintained at a few pounds above ambient

pressure, the differential pressure (DP) is very low. For low DPs, the added load is very low. Additionally, seals that operate with high differential pressure are prone to slight leakage. Any leakage of seawater over an extended period of time can result in failure of electric devices. For these reasons, shaft seals with high differential pressure should be avoided in this application, and a pressure tolerant motor should be used.

The disadvantage of the pressure tolerant motor is an increased loss of power due to windage. The windage comes from the fluidic drag on the rotor of the motor due to the presence of a fill fluid. The fill fluid is a non-conductive fluid maintained at a few psi above ambient pressure and it surrounds and fills the motor. This prevents the highly conductive and corrosive seawater from entering the motor.

Since ABE is a battery powered vehicle with a bus voltage of 48 VDC, a DC motor is the obvious choice for the prime mover of the thruster.

The transmission must be selected to match the motor, which is most efficient at high speeds, to the propeller, which has high efficiency at lower speeds. The gearbox must also be of sufficiently high quality and precision to minimize the losses due to the gearing.

3.2 DC Brushless Motors

3.2.1 Brushed versus Brushless Motors

DC motors come in two main types: Brushed and Brushless. Brushed motors are the most common DC motor. They have a mechanical arrangement of split rings and brushes called a commutator. The commutator switches the voltage applied to the coils depending on the position of the rotor. This switching keeps a positive force on the rotor to keep it rotating. A brushless motor relies on electronics to provide the proper commutation to the motor based on feedback from an external rotor position detector.

In a high pressure environment, spring loaded brushes experience increased wear and a tendency to hydroplane on the non-conductive fill fluid. The hydro-planing leads to brush chatter and an increased heat load due to the increased electrical resistance. Brushed motors have a short life expectancy in the high pressure environments.

Since the commutation on brushless motors is accomplished electronically, they do not suffer from any of the above problems. They are, however, much more expensive and require complicated (and expensive) controllers. Due to the importance of longevity and reliability in ABE's mission environment, DC brushless motors will be used.

3.2.2 Motor Equations

In order to evaluate the motor, the efficiency of the motor is calculated. The motor chosen for ABE is a Pittman elcom © 5100 series DC brushless motor. This motor was chosen for size and rated capacity. A schematic of the motor, defining the variables used in the equations, is shown in Figure 3.1 .

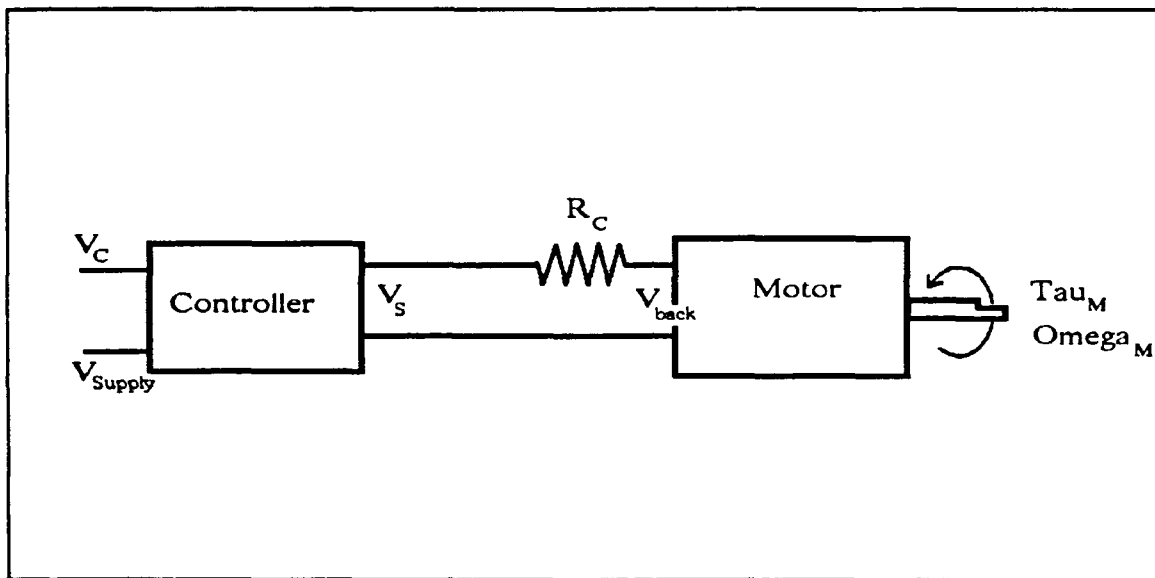


Figure 3.1 Motor Schematic

The motor constants and parameters for this motor are:

Torque Constant: $K_T = 0.173 \text{ Nm/Amp}$

Back EMF Constant: $K_E = 0.173 \text{ V/(rad/sec)}$

Coil Resistance: $R_C = 4.85 \text{ ohms}$ [5]

For steady state operation, the following equations describe the operation of a DC motor:

$$\text{Back EMF:} \quad V_{\text{BACK}} = K_E \omega_m$$

$$\text{Motor Torque:} \quad \tau_m = K_T I_m$$

$$\text{Motor Current:} \quad I_m = (V_S - V_{\text{BACK}}) / R_C$$

Where V_S is the supply voltage and ω_m is the angular velocity of the rotor. Efficiency can be calculated as:

$$\eta_m = \frac{P_{\text{out}}}{P_{\text{in}}} = \frac{\tau_m \omega_m}{V_S I_m} \quad (3.1)$$

From equation 3.1, it can be seen that efficiency increases with motor speed. This neglects the effect of windage which increase with speed.

3.3 The Fill Fluid and Windage

The fluid used for compensation is Halocarbon © 0.8 cSt fluid. This is a silicon oil based fluid with a viscosity 20% less than water. Of the commercially available, non-conductive fluids, this fluid provides pressure compensation and has the lowest viscosity. For the purposes of efficiency calculation, the fluid flow around the rotor will be considered to be laminar flow between two parallel surfaces. From testing of other motors with this fluid, a linear relationship exists between torque due to drag and angular velocity. The proportionality constant in this relationship

is $K_w = 5.175 \times 10^{-5} \text{ Nm/(rad/sec)}$. The torque lost (τ_w) and the power lost (P_w) due to windage are: [6]

$$\tau_w = K_w \omega_m \quad \text{and} \quad P_w = K_w \omega_m^2$$

3.4 The Gearbox

Gearboxes are available in a wide variety of types, gear-ratios and efficiency. Gearbox efficiency is highly dependent on the manufacturer's tolerances and construction procedures. For the Pittman motors, a variety of planetary gearboxes are available. These gearboxes will be used to determine the desired gear ratio for the ABE thruster. In order to calculate the desired gear ratio, descriptive equations of the performance of the gearbox must be determined. The equations must be written in terms of gear ratio.

To formulate the equations it is assumed that a planetary gearbox is made up of an arbitrarily small stage. A certain number of these stages are stacked in order to get the desired reduction ratio. Each stage has a specific gear reduction (1.1:1) and a specific efficiency (η_i). The complete gearbox then has a gear reduction ratio of $(1.1)^n:1$ and an efficiency of η_i^n where n is the number of stages (including fractional stages) needed to get the desired reduction. For the Pittman gearboxes, two advertised gearboxes are a 4:1 and a 17.33:1 gear ratio with efficiencies of 80% and 64% respectively. If the 4:1 gearbox is used as a baseline, $n=14.545$ and $\eta_i=0.985$.

If these numbers are used to calculate the efficiency for the 17.33:1 gearbox, $n=29.93$ and the efficiency is 63%. Since this is a good match, the following equations will be used to describe the gearbox:

$$N = (1.1)^n \quad \text{AND} \quad \eta_G = (0.985)^n \quad (3.3)$$

3.5 Matching the Motor with the Propeller

In order to evaluate a proper match between the propeller and the motor, a set of equations describing the motor, windage and gearbox must be evaluated for various gear ratios. Combining the optimum propeller RPM and torque from chapter 2 with the component equations developed above, a system can be evaluated. Figure 3.2 shows the block diagram of the system.

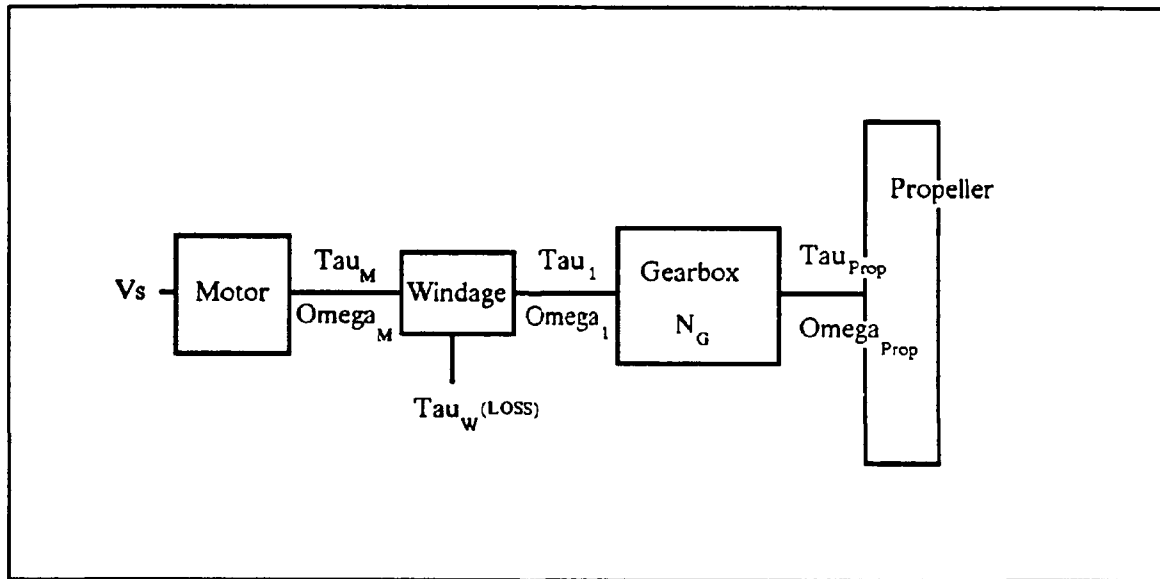


Figure 3.2 Thruster System Block Diagram

The descriptive equations are:

$$\tau_{prop} = 0.46 \text{ ft lbf} = 0.62386 \text{ Nm}$$

$$\omega_{prop} = 94.5 \text{ RPM} = 9.896 \frac{\text{rad}}{\text{sec}}$$

$$\tau_1 = \frac{\tau_{prop}}{N_G \eta_G} \quad \omega_1 = N_G \omega_{prop}$$

$$\tau_m = \tau_1 + \tau_v \quad \tau_v = K_v \omega_m$$

$$\omega_m = \omega_1 \quad I_M = \frac{\tau_m}{K_T}$$

$$V_S = V_{BACK} + R_T I_m \quad V_{BACK} = K_E \omega_m$$

$$N_G = (1.1)^n \quad \eta_G = (.985)^n$$

$$K_T = 0.173 \frac{\text{Nm}}{\text{Amp}} \quad K_E = 0.173 \frac{\text{Volt}}{(\frac{\text{rad}}{\text{sec}})}$$

$$K_v = 5.175 \times 10^{-5} \frac{\text{Nm}}{(\frac{\text{rad}}{\text{sec}})}$$

These equations reduce to:

$$V_s = K_E (1.1)^n \omega_{prop} + R_T I_m$$

$$I_m = \frac{T_{prop}}{(1.1)^n K_T (0.985)^n} + (1.1)^n \omega_{prop}$$

with the component efficiencies defined by the following:

Motor efficiency without windage:

$$\eta_m = \frac{\text{Power out}}{\text{Power in}} = \frac{\tau_m \omega_m}{V_s I_m}$$

Motor efficiency with windage:

$$\eta_{mw} = \frac{\text{Power out}}{\text{Power in}} = \frac{\tau_m \omega_m + \tau_w}{V_s I_m}$$

Gearbox efficiency:

$$\eta_G = (0.985)^n$$

Total system efficiency:

$$\eta_T = \eta_{mw} \eta_G$$

These efficiencies were calculated for various gear ratios. Figure 3.3 shows a plot of these efficiencies and Figure 3.4 shows an enlargement of the total efficiency curve. By inspection of this figure, the ideal gear ratio is about 10:1.

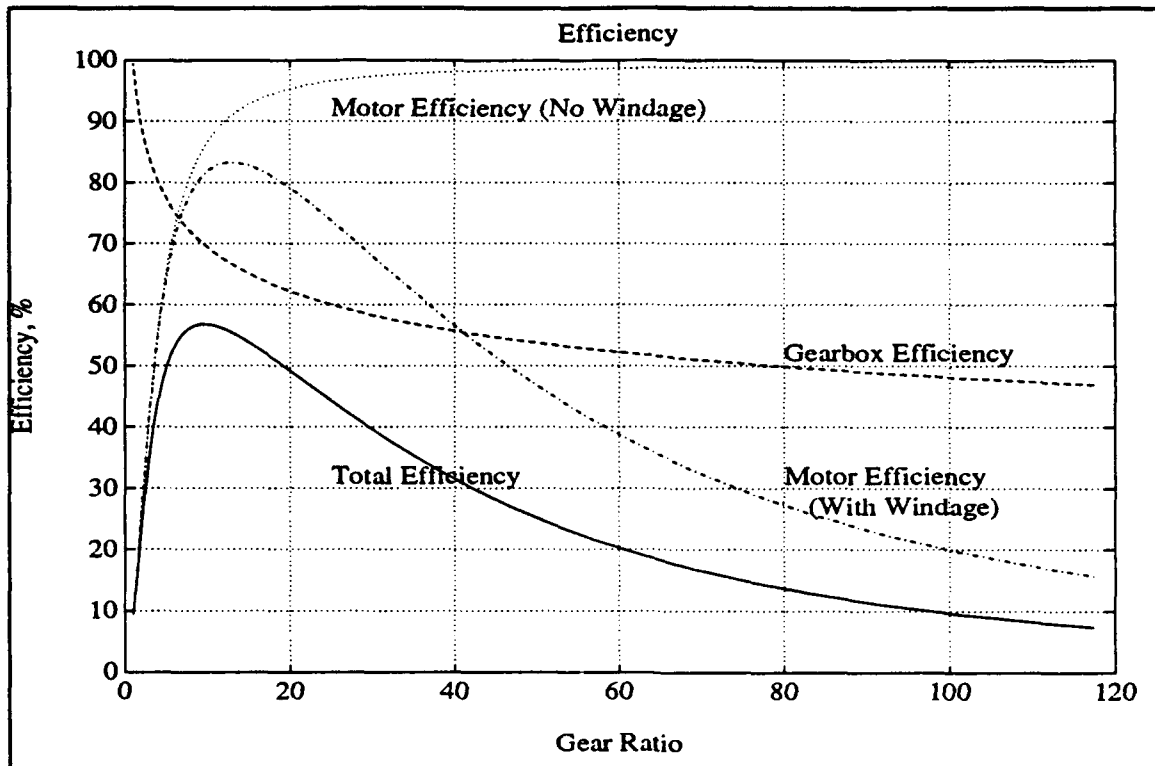


Figure 3.3 System Efficiencies

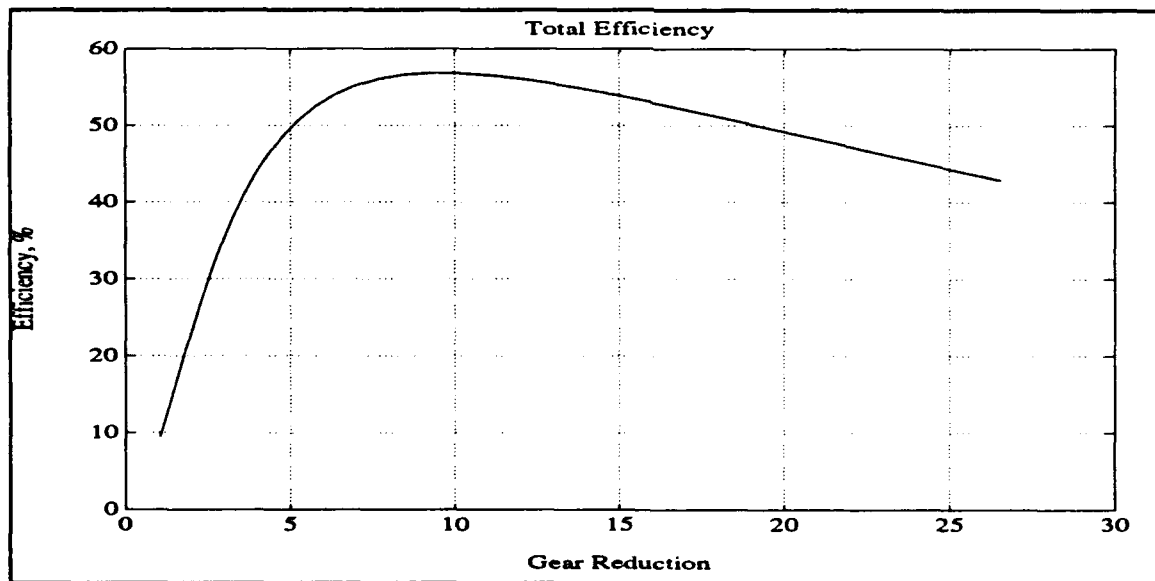


Figure 3.4 Total System Efficiency

3.6 Sensitivity of the Analysis

This analysis was carried out using several different stage reduction ratios and efficiencies. The effects of changing these parameters are summarized below.

1. Changing the stage reduction ratio only from 1.1:1 to 4:1 had little effect on the gear ratio where the peak efficiency occurred. It did effect the height of the peak significantly.

2. Varying the stage efficiency alone (fixed 1.1:1 stage reduction ratio) had little effect on the peak location while the stage efficiency was above 95%. Below 95% the peak moved to lower gear ratios.

3. Varying both the stage reduction ratio and efficiency in a coordinated manner to maintain 80% efficiency at a 4:1 gear ratio, had no significant effect on both peak location and height.

In general, the model of the gearbox and motor developed in this chapter is relatively insensitive to the assumptions made about the gearbox. The windage loss dominates the peak efficiency curve, provided a gearbox with sufficiently high efficiency is used.

Chapter 4

The Lumped Parameter Model of The Propulsor

4.1 Introduction

ABE will incorporate a complex control system designed to allow the vehicle to operate independently for periods of up to twelve months. In order to accomplish this mission, ABE must have extremely efficient thrusters and an efficient control algorithm. The control algorithm must be based on a simple, yet accurate model of the thruster. In this chapter a lumped parameter model of the thruster is developed and presented in bond graph notation. A simulation of this model was performed using MATLAB, and the results are compared to experimental data in Chapter 5.

4.2 Description of the Thruster Unit

The thruster under consideration, consists of a DC brushless motor, a controller for the motor, a 10:1 reducing gearbox, a three blade propeller mounted in a duct. Figure 4.1 shows a schematic diagram of this assembly.

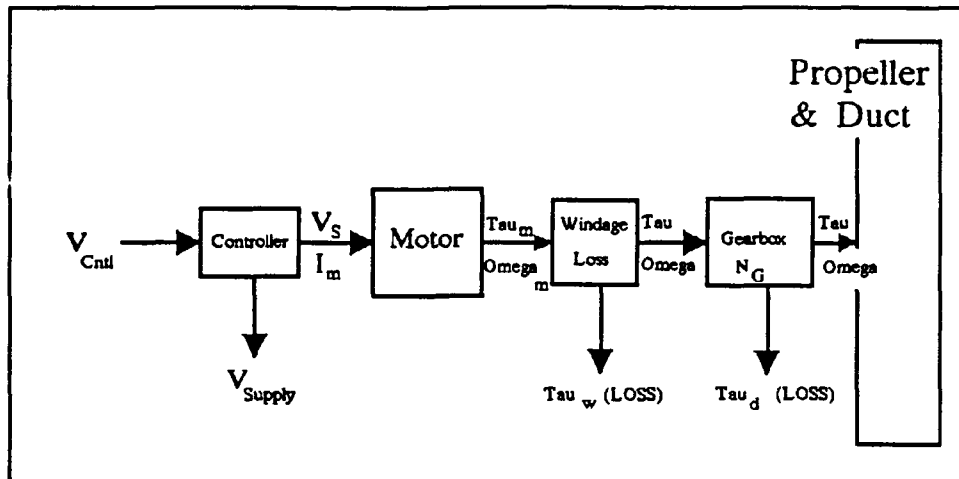


Figure 4.1. Schematic representation of the thruster unit.

4.2.1 The Propeller and Duct Assembly

The propeller and duct assembly as a unit, has the single most significant impact on the overall efficiency of the thruster. Therefore, the model of this unit determines the accuracy and utility of the overall model. Figure 4.2 shows the schematic representation of the propeller and duct. In order to describe the hydrodynamic relationships, the following simplifying assumptions are made [7]:

1. The ambient fluid is inviscid, incompressible and of constant density.
2. The gravity effects on the fluid are negligible.

3. The flow at the inlet and outlet is parallel to the thruster axis. (irrotational).
4. The only energy storage in the fluid is by kinetic energy.
5. The kinetic energy of the ambient fluid is negligible.
6. The ambient pressure is P_0 and it acts equally at the inlet and the outlet.

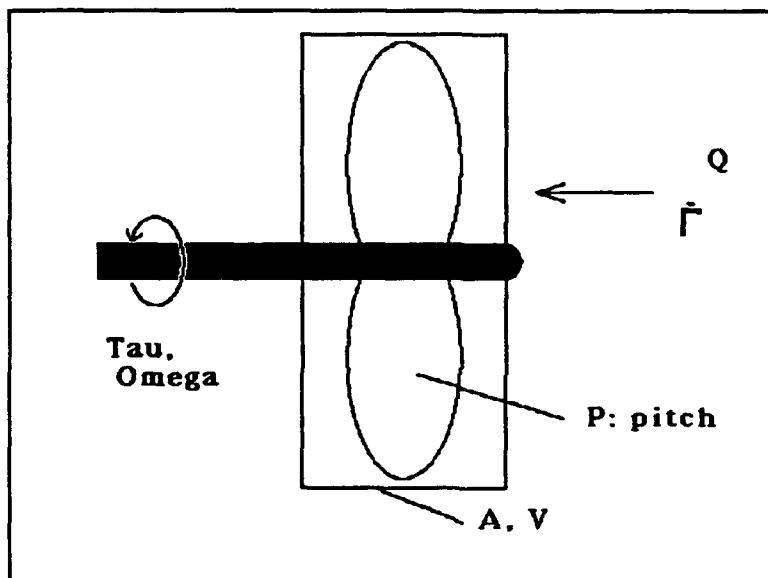


Figure 4.2. The propeller and duct assembly, Schematic Representation.

In order to model the hydrodynamics, first, consider the Kinetic Co-energy, E_K^* . This is the typical "Physics Book Kinetic Energy" $\{ \frac{1}{2} m v^2 \}$.

$$E_K^* = \frac{1}{2} (\rho V) \left(\frac{Q}{A} \right)^2 \quad (4.1)$$

Where ρV is the mass of the fluid enclosed by the duct. However, this volume must be corrected to take account of the

added mass effect of the surrounding fluid. This correction involves a concept known as Added Mass or Virtual Mass. Added mass is a phenomenon that occurs when a body (or a fluid element) moves through a fluid. An additional inertia effect is added to account for the effort required to "push" the fluid out of the way of the moving body. For the case of a body moving slowly through a static fluid, the added mass is equal to the volume of the body times the density of the fluid (ie. the mass of the displaced fluid) [8] and [9]. For this model (where the density is constant) this is done by setting V to twice the actual enclosed volume. Q is the volumetric flow rate. A is the cross-sectional area of the duct. Now, define the pressure momentum, Γ , as:

$$\Gamma \triangleq \frac{d}{dQ}(E_K^*) = \frac{\rho V Q}{A^2} \quad (4.2)$$

***Note that there is a linear relationship between Γ and Q . This is analogous to the standard translational definition of momentum, $p=mv$, and leads to the numerical equality of the Kinetic Energy, E_K and the Kinetic Co-energy:

$$E_K^* = \int \Gamma dQ = \frac{1}{2} \rho V \left(\frac{Q}{A} \right)^2 \quad (4.3)$$

$$E_K = \int Q d\Gamma = \int \frac{A^2 \Gamma}{\rho V} d\Gamma = \frac{A^2 \Gamma^2}{2 \rho V} = \frac{A^2}{2 \rho V} \left[\frac{\rho V Q}{A^2} \right]^2 = \frac{\rho V Q^2}{2 A^2} = E_K^*$$

In Summary:

$$E_K = E_K^* = \frac{\rho V Q^2}{2 A^2} = \frac{A^2 \Gamma^2}{2 \rho V} \quad (4.5)$$

$$\Gamma = \frac{\rho V Q}{A^2} \quad \text{And} \quad Q = \frac{A^2 \Gamma}{\rho V} \quad (4.6)$$

Now consider a power balance for the propeller and duct.

Power in:

The power flow into the duct comes from three major components: 1) The driving motor, 2) Any Kinetic Energy flowing into the thruster inlet, and 3) The velocity/opposing-force product at the inlet (work done by the fluid entering).

1. The power input from the motor/gearbox is the product of the torque, τ , and the angular velocity, ω .

2. Since it is assumed that the ambient fluid is at rest, there is no kinetic energy flow into the thruster.

3. The velocity/force power is the product of ambient pressure P_0 and the cross-sectional area and the fluid velocity at the inlet.

$$P_{in} = \tau \omega + (P_o A) \left(\frac{Q}{A} \right) + E_{K-in} = \tau \omega + P_o Q \quad (4.7)$$

Power out:

The power flows out of the duct by two processes. The first is the force/velocity work at the discharge. The second is the kinetic energy of the discharged fluid. This latter flow is called the convected kinetic energy.

1. Since the cross-sectional area is constant and the average velocity of the fluid is the same at the inlet and outlet, this term is the same as the corresponding term at the inlet, $P_o Q$.

2. The convected kinetic energy is the kinetic energy per unit volume times the volumetric flow rate:

$$K = \text{Convected Kinetic Energy} = \frac{E_K}{V} |Q| = \frac{A^2 \Gamma^2 |Q|}{2 \rho V^2} \quad (4.8)$$

$$P_{out} = P_o Q + \frac{A^2 \Gamma^2 |Q|}{2 \rho V^2} \quad (4.9)$$

Note: the absolute value preserves the sign of the convected kinetic energy to allow for flow reversal.

Balance of Power:

The net rate of change of the energy in the fluid contained in the duct is equal to $P_{in} - P_{out}$.

$$\frac{d}{dt} E_T = P_{in} - P_{out} = \tau \omega + P_o Q - P_o Q - \frac{A^2 \Gamma^2 |Q|}{2 \rho V^2} = \tau \omega - \frac{A^2 \Gamma^2 |Q|}{2 \rho V^2}$$

Since the only method of energy storage within the duct is through kinetic energy:

$$\frac{d}{dt} E_T = \frac{d}{dt} E_K = \frac{d}{dt} \left(\frac{A^2 \Gamma^2}{2 \rho V} \right) = \frac{A^2 \Gamma}{\rho V} \dot{\Gamma} = \tau \omega - \frac{A^2 \Gamma^2 |Q|}{2 \rho V^2} \quad (4.11)$$

This leads to the first state equation:

$$\dot{\Gamma} = \frac{\rho V \tau \omega}{A^2 \Gamma} - \frac{\Gamma |Q|}{2 V} \quad (4.12)$$

However, $Q=Q(\Gamma)=Q(\omega)$ therefore we can write Γ as $\Gamma(\omega)$ and reduce equation (12) as follows:

1. Define p as the pitch of the propeller. This quantity is also known as the advance of the propeller. Specifically, p is the distance the propeller travels axially per revolution in an "ideal" fluid.

2. Define η , the propeller's efficiency, is equal to $1-\sigma$; where σ is the slip of the propeller: [7]

$$\sigma \triangleq \frac{\omega p A - 2\pi Q}{\omega p A} \quad (4.13)$$

Now we can write Γ and Q in terms of ω .

$$Q = \frac{\omega p \eta A}{2\pi} \quad (4.14)$$

where $Q = (\text{rev per sec}) * (\text{pitch}) * (\text{efficiency}) * (\text{Area})$
 $= \text{Volumetric Flow rate}$

$$\Gamma = \frac{p \eta \rho V \omega}{2\pi A} \quad (4.15)$$

Using equations (4.6) and (4.15), we can rewrite equation (4.12) as:

$$\Gamma = \frac{2\pi\tau}{p\eta A} - \frac{A^2\Gamma|\Gamma|}{2\rho V^2} = \frac{2\pi\tau}{p\eta A} - \frac{pQ|Q|}{2A^2} \quad (4.16)$$

This equation can easily be written in terms of ω :

$$\dot{\omega} = \frac{4\pi^2\tau}{p^2\eta^2\rho V} - \frac{p\eta A\omega|\omega|}{4\pi V} \quad (4.17)$$

From these equations we get the bond graph shown in Figure 4.3.

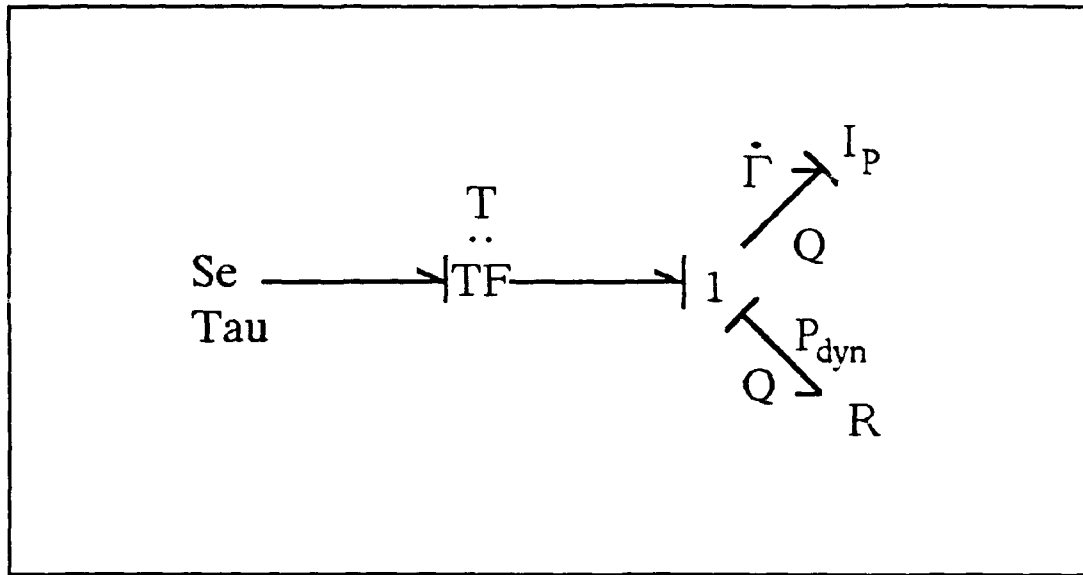


Figure 4.3. Bond Graph for Propeller-Duct Assembly.

The Equations for the Propeller and duct are:

$$\dot{\Gamma} = \frac{2\pi\tau}{p\eta A} - P_{dyn} \quad (4.18)$$

$$R \text{ is Defined such that } P_{dyn} = \frac{\rho Q|Q|}{2A^2} \quad (4.19)$$

$$Q = \frac{A^2\Gamma}{\rho V} \quad I_P = \frac{\rho V}{A^2} \quad (4.20)$$

$$\omega = \frac{2\pi Q}{p\eta A} \quad T = \frac{2\pi}{p\rho A} \quad (4.21)$$

The dissipator (R) is often referred to as a "Bernoulli Resistor". In this model, the convected kinetic energy is dissipated to the ambient fluid. By assuming that the ambient fluid remains at rest, it is assumed that the ambient fluid

acts as an infinite sink for this energy, much the same as is considered for the thermal energy dissipated by an electrical resistor [10].

The parameters for the propeller are: $p=0.41$ meters/rev., Propeller efficiency is 60%, $A= 0.164 \text{ m}^2$, corrected volume is 0.033 m^3 .

4.2.2 The Gearbox

The motor is connected to the propeller shaft by means of a gearbox. This gearbox has a planetary gear arrangement yielding a 10:1 reduction of speed. This gearbox is necessary to increase overall efficiency since the motor operates most efficiently at high speeds and the propeller operates best at lower speeds. The gearbox arrangement is shown in Figure 4.4.

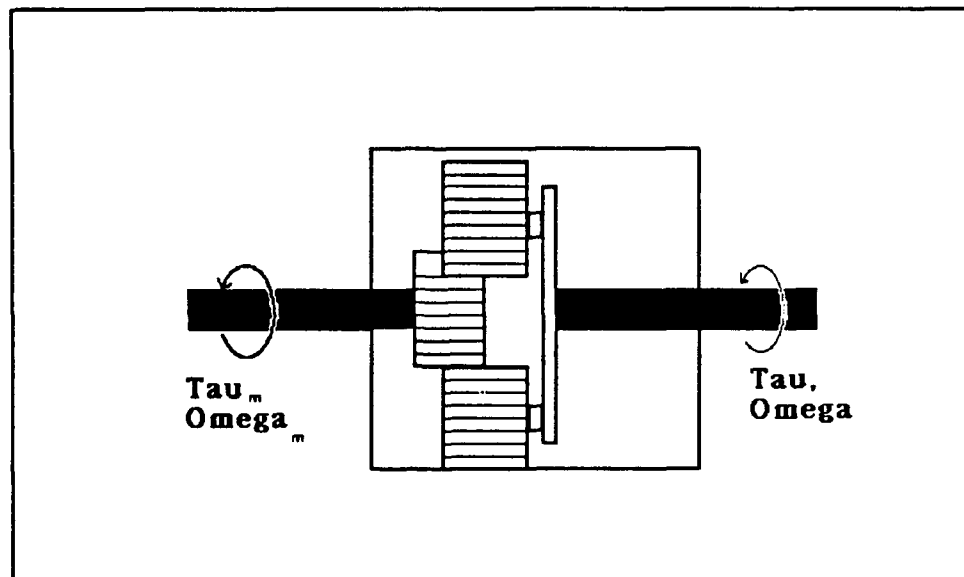


Figure 4.4. Gearbox Schematic Diagram

The gearbox used has an 80% efficiency at top speed (input shaft maximum speed is 10,000 RPM). This means that there is a dissipative element as well as a torque multiplication. The inertial load of the gearbox will be included with the motor's rotor inertia. Defining τ_m as the motor output torque, τ_1 as the gearbox output torque, ω as the input shaft speed, and ω_1 as the output shaft speed, the gearbox can be modelled as shown in the block diagram of Figure 4.5 .

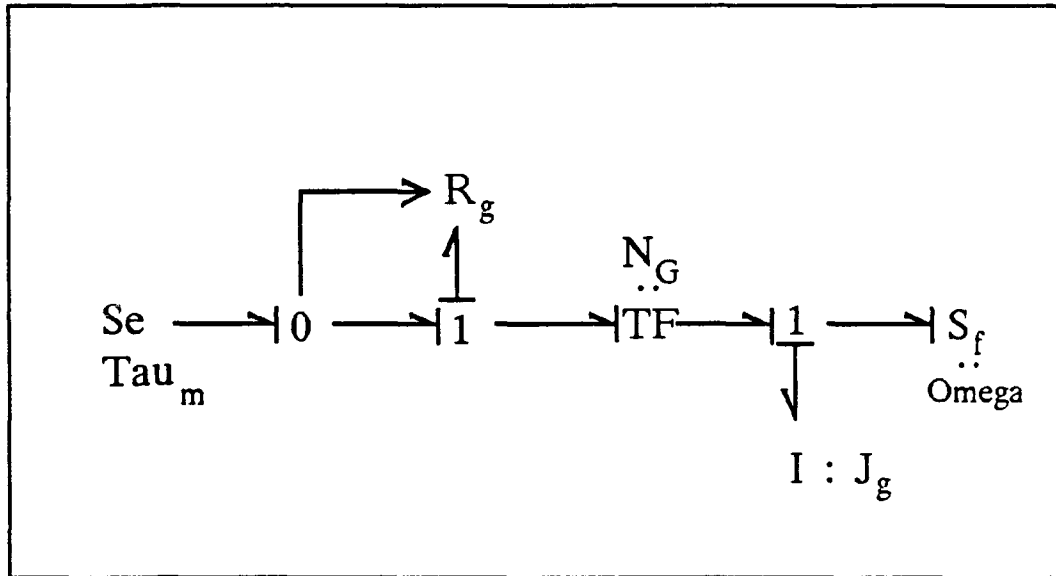


Figure 4.5. Bond Graph for Gearbox.

The equations describing the gearbox are:

$$R_G = \frac{0.2 \tau_m}{\omega_{\max}} \quad N_G = 10 \quad (4.22)$$

$$\tau = N_G (\tau_m - \tau_d) \quad \tau_d = \frac{0.2 \tau_m \omega_m}{\omega_{\max}} \approx 0.2 \tau_m \quad (4.23)$$

J_G will be combined with other inertias into an equivalent inertia.

4.2.3 The Motor

The motor used is a Pittman elcom © DC Brushless motor. It is controlled using a ± 10 VDC control voltage and a supply voltage ranging from 30 to 80 Volts DC. In this application the supply voltage is chosen to be 48 VDC. In order to simplify the model, the supply and control voltages are "tied" together. This idealizes the controller portion of the model by assuming no losses in the amplification. The motor diagram is shown in Figure 4.6 .

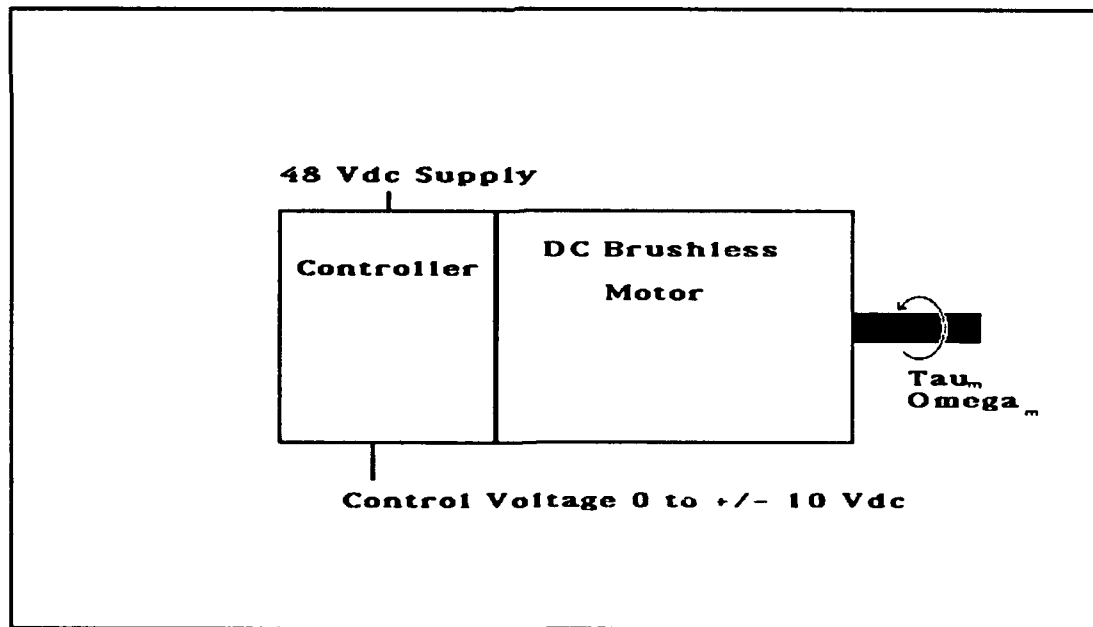


Figure 4.6. The Motor Assembly.

In order for the motor to operate on the ocean floor, it must be surrounded by a non-conductive fluid that is compensated to be at the same pressure as the environment (10,000 psi). The fluid in use is a silicon based oil called Halocarbon © 0.8 cSt. This oil adds a significant windage loss to the motor ($\approx 5.2 \times 10^{-5}$ Nm/(rad/sec)).

The motor is then modelled by Gyrator, a mechanical inertia and dissipator, and an electrical resistance and inductance.[11] The gyrator constant is 0.173 Nm/Amp or 0.173 V/(rad/sec). The stator resistance $R_T=4.85 \Omega$, the stator inductance $L_m= 1.65$ mH, the combined rotor and gearbox moment of inertia $J_r=38.6 \times 10^{-6}$ Kg m². These numbers are from the manufacturer's specifications. The resulting bond graph is shown in Figure 4.7 .

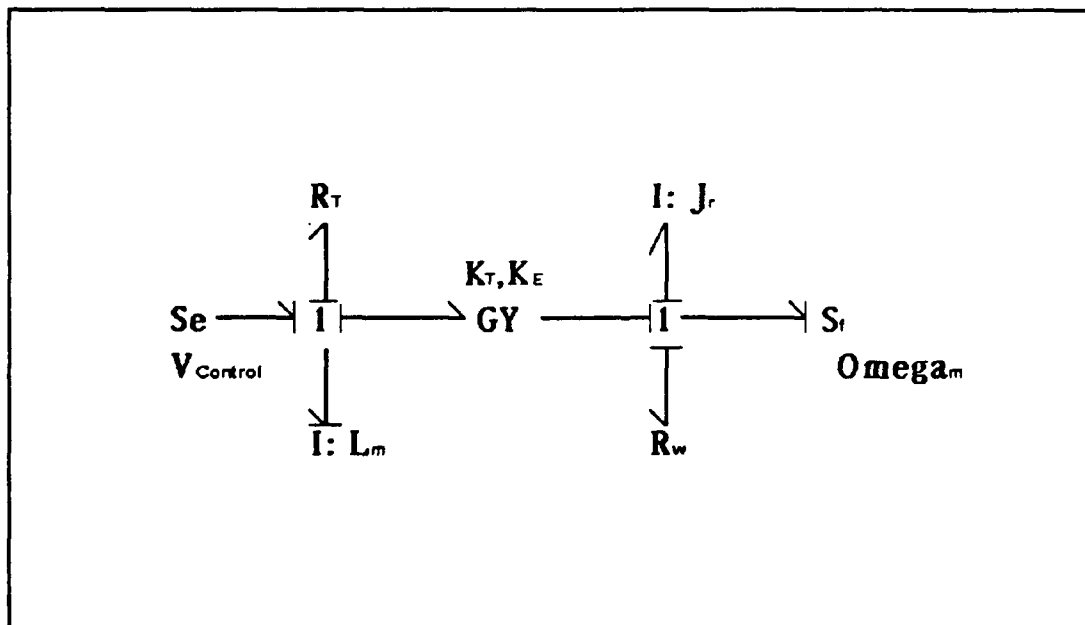


Figure 4.7. The motor bond graph.

The resulting equations model the motor:

$$\tau_m = \tau_1 - J_r \dot{\omega}_m - R_w \omega_m \quad (4.24)$$

$$\tau_1 = K_T I_m \quad (4.25)$$

$$V_{back} = K_E \omega_m \quad (4.26)$$

$$\dot{I}_M = \frac{1}{L_c} [V_{control} - V_{back} - R_T I_M] \quad (4.27)$$

4.3 The Complete Thruster Model

The complete model is shown in Figure 4.8 .

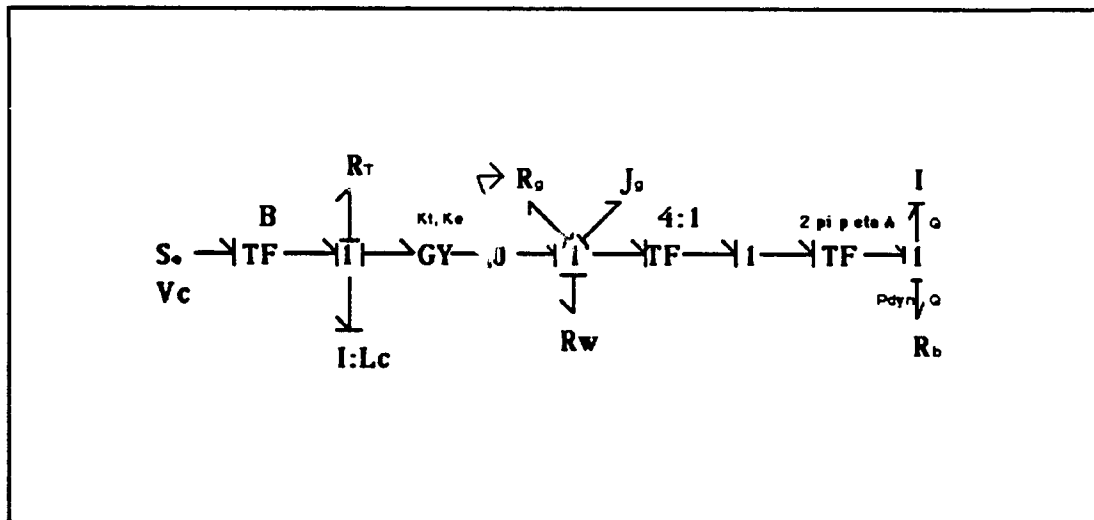


Figure 4.8

In summary the equations are:

$$\dot{\Gamma} = \frac{2\pi\tau}{p\eta A} - P_{dyn} \quad \text{or} \quad \dot{\omega} = \frac{4\pi^2\tau}{p^2\eta^2\rho V} - \frac{p\eta A\omega|\omega|}{4\pi V}$$

$$P_{dyn} = \frac{\rho Q|Q|}{2A^2}$$

$$Q = \frac{A^2\Gamma}{\rho V}$$

$$\omega = \frac{2\pi Q}{p\eta A}$$

$$\tau = N_G(\tau_m - \tau_d) \quad N_G = 10$$

$$\tau_d = \frac{0.2\tau_m\omega}{\omega_{max}}$$

$$\omega_m = N_G\omega$$

$$\tau_m = K_T I_m - J_r \dot{\omega}_m - R_w \omega_w$$

$$V_{back} = K_E \omega_m$$

$$\dot{I}_m = \frac{1}{L_c} [V_{control} - V_{back} - R_T I_m]$$

The output of the system is thrust. Thrust is equal to the time rate of change of momentum. For our system the thrust is equal to the convected momentum, specifically, the product of momentum per unit volume and the volumetric flow rate.

$$\text{Thrust} = (\text{momentum per unit volume}) Q = \left| \frac{A\Gamma}{V} \right| Q = \frac{A^3 \Gamma |\Gamma|}{\rho V^2}$$

Thrust can also be written in terms of ω :

$$\text{Thrust} = \frac{Ap^2\eta^2\rho\omega|\omega|}{4\pi^2}$$

The bond graph representation of Figure 4.8 can be put into block diagram form. The resulting block diagram of the complete thruster unit is shown in Figure 4.9.

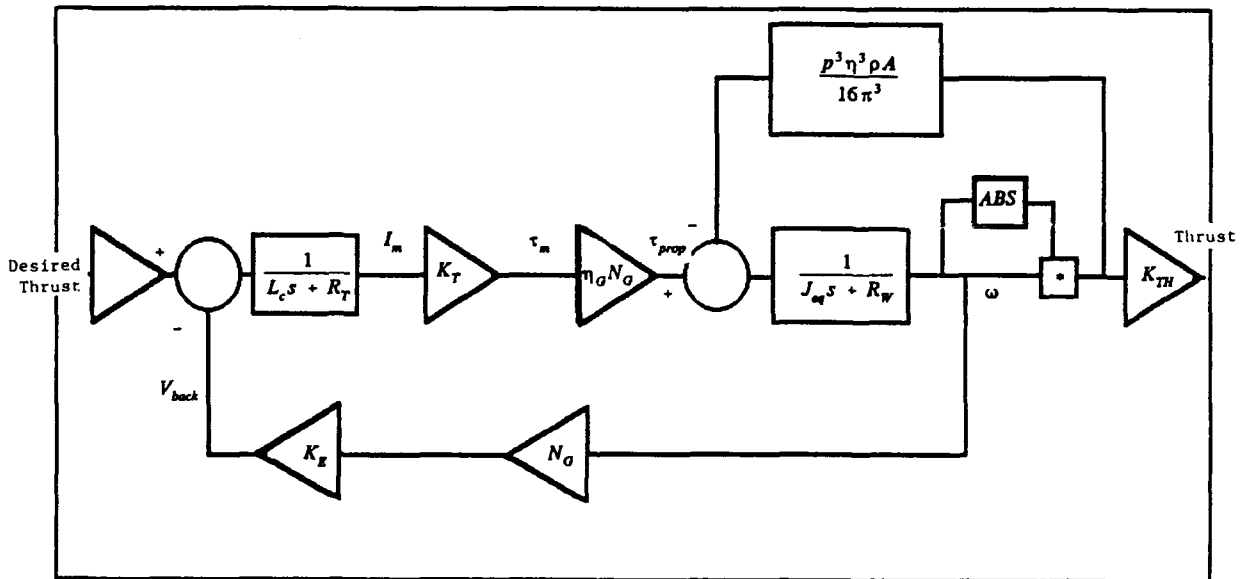


Figure 4.9 The Complete Model Block Diagram

This model contains the electrical dynamics of the motor as well as the hydrodynamics of the propeller. The electric time constant $L_c/R_T = 0.34$ milliseconds. This is extremely fast compared to the hydrodynamic time constant which is on the order of a second. Therefore the hydrodynamics dominate the electrical and the latter can be neglected without degrading the model. The resulting model is shown in Figure 4.10. The model presented here has been simplified to correspond to the model used in reference [12].

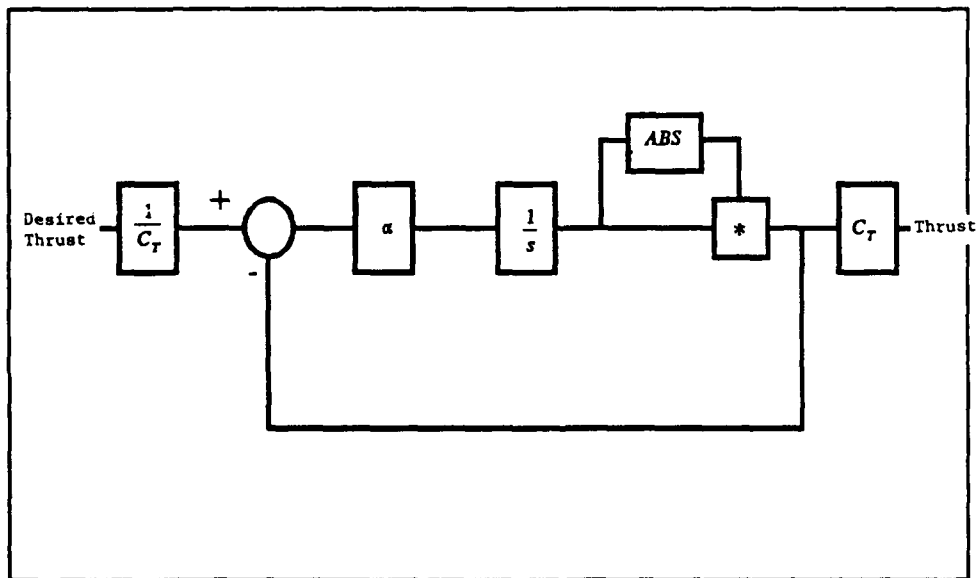


Figure 4.10 The Simplified Model Block Diagram

Where R_w is neglected since $R_w \ll J_{eq}$ and:

$$C_T = \frac{Ap^2\eta^2\rho}{4\pi^2} \quad , \quad \alpha = \frac{p^3\eta^3\rho A}{16\pi^3 J_{eq}}$$

and Torque = βV_c and Power = $\tau\omega = \beta V_c\omega$ where β is a motor constant with units of Newton Meters per Volt.

4.4 Simulation

The model of Figure 4.10 was used in MathWorks© MATLAB™ program. This program was used to simulate the response of the thruster to various inputs. The results of these simulations are compared with experimental data in Chapter 5.

4.5 Summary

In this chapter, a lumped parameter model was developed to describe a underwater vehicle thruster unit. From this lumped parameter model, a simplified block diagram model was derived. This model will be used to predict the response of an actual thruster unit under test at the Woods Hole Oceanographic Institution. The three parameters of the final model (C_T , α , and β) will be calculated and then tuned to get the best match between the actual response and the simulated response.

Chapter 5

Experimental Verification

The next consideration is to show that the model developed in Chapter 4 is competent to describe the actual thruster. This will be done in three steps. First, by equating the steady state responses of the model and the experimental thruster. Second, the model will be tuned to match the thrusters step response. Finally, the actual and predicted responses to several frequencies of sinusoid will be examined. The model's ability to correctly predict the sinusoidal response will be evaluated.

5.1 The Experimental Setup

For the purposes of model verification, an MFM™ DC brushless motor (electrically comparable to the Pittman motor described in Chapter 4) with a 10:1 gearbox, was mounted in a housing filled with Halocarbon fluid. The experimental propeller (Michigan Wheel 3-blade 16-inch pitch propeller) was mounted on the gearbox output shaft and supported radially by an external journal bearing. A frame was constructed to hold the motor housing and bearing assembly. The frame is

supported at a single pivot point with a lever arm extending upward to allow force measurement to occur out of the water. Figure 5.1 shows the arrangement of the frame and the force measurement sensor. The force sensor is an S-type load cell rated at 500 pounds-force.

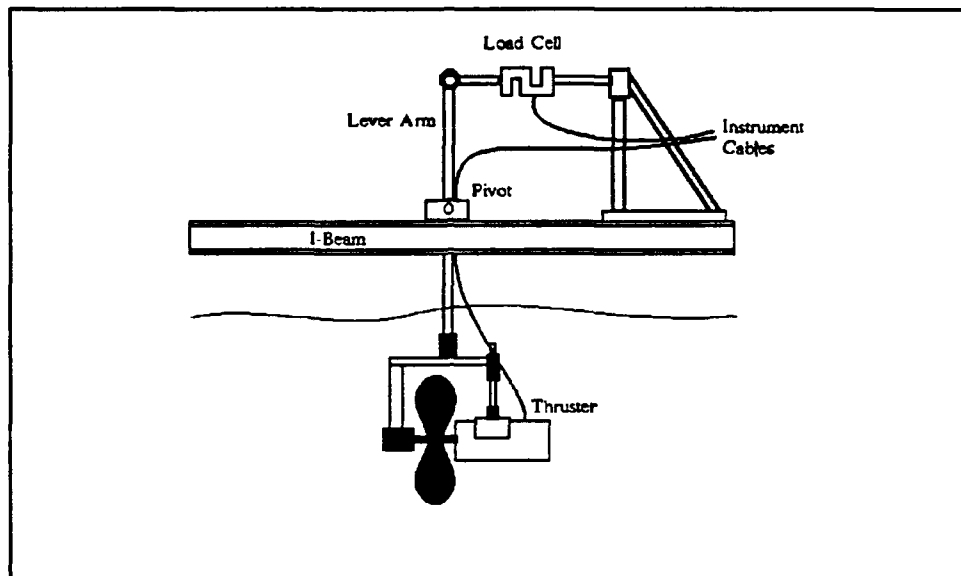


Figure 5.1 The Experimental Test Stand

After initial testing, the test frame was reinforced to reduce the oscillatory effect of the vertical lever arm compliance. This reinforcement significantly reduced the "ringing" of the thrust measurement. In order to remove gravity effects, the test assembly was balanced before each data run, so the vertical lever arm was straight up and down. The force sensor was arranged to measure the horizontal component of force at the end of the vertical arm. This arrangement decouples all gravitational effects of the motor and propeller from the force measurement.

5.2 Steady State Response

The constants of the model developed in Chapter 4, (C_T , α , and β) were adjusted so the model accurately predicts the correct steady state response of the thruster for thrust, angular velocity, and power input required. This process determined C_T and β directly.

5.3 Step Response

The step response data collected with the experimental thruster was used to determine the α parameter. The modelled response to three separate step inputs is shown in Figure 5.2 and the actual response is shown in Figure 5.3 (a,b,&c).

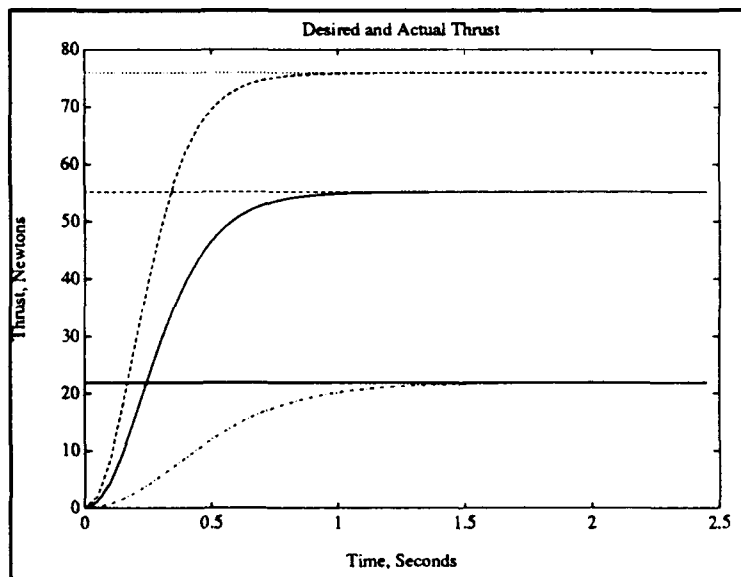


Figure 5.2 Model Step Response

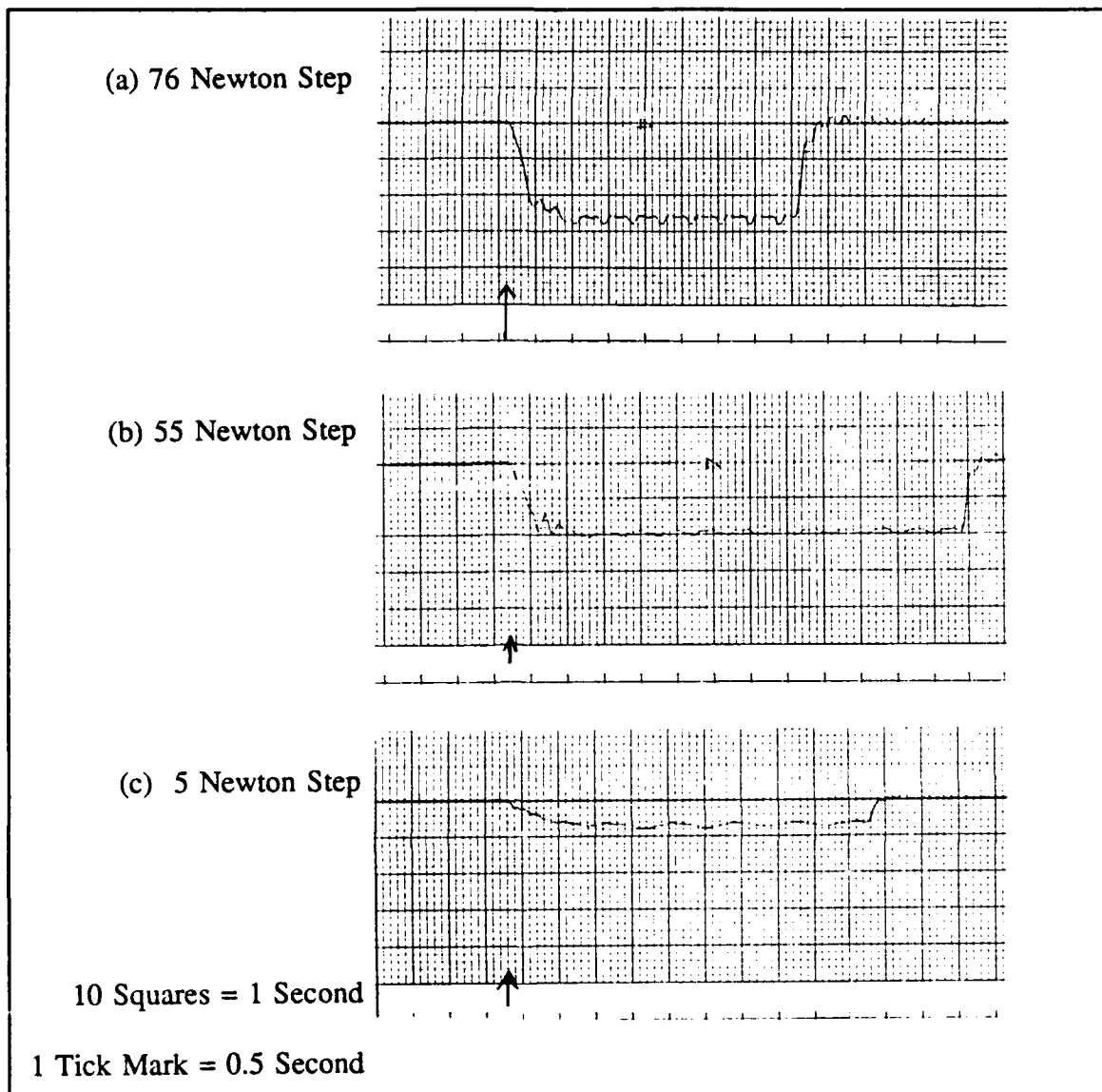


Figure 5.3 Actual Thruster Step Response

5.4 Sinusoidal Response

The model and the actual thruster were given sinusoidal inputs of five different frequencies between 0.1 Hz and 1.6 Hz. The model response is shown in Figures 5.4 through 5.8

sub-plot (a). The actual response is shown in subplot (c) of the same figures. Note that the actual response is inverted. The time scale is .1 second per finest square. The force scale is 5.7 N per smallest division.

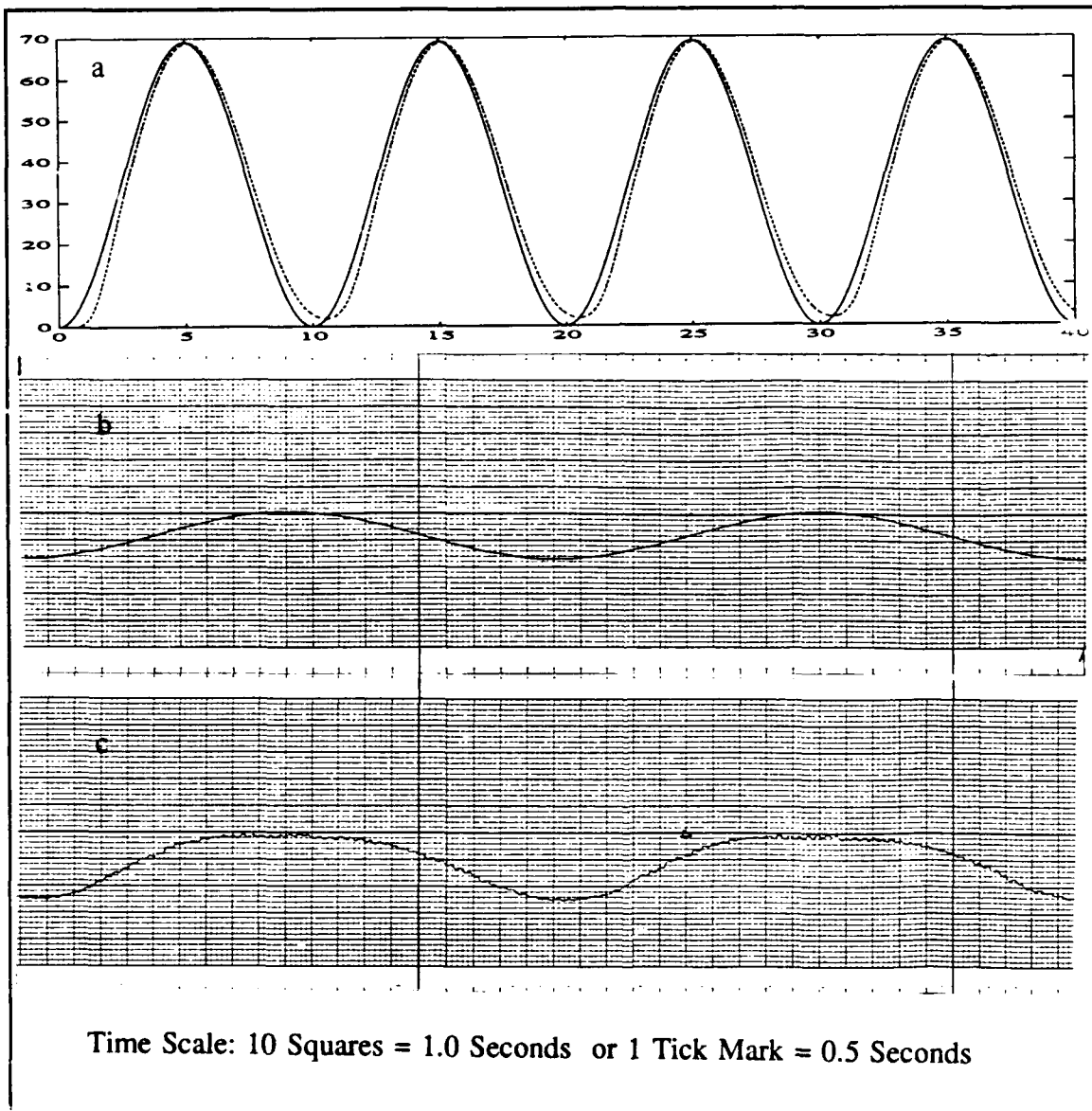


Figure 5.4 Sinusoidal Input $T=10$ seconds. (a) Model Input and Response, (b) Actual Input, (c) Actual Response

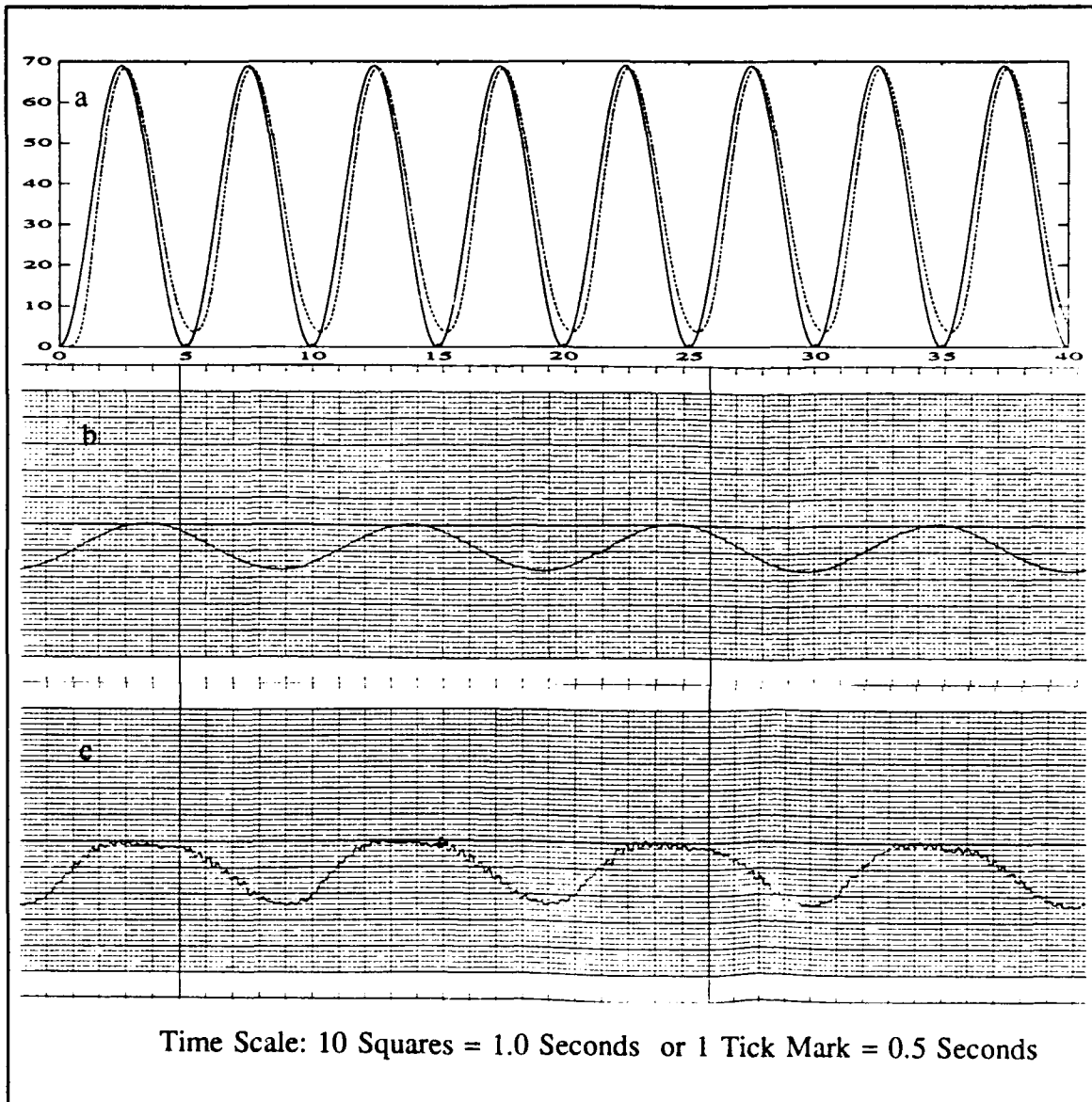


Figure 5.5 Sinusoidal Response, $T=5.0$ Seconds, (a) Model Input and Response, (b) Actual Input, (c) Actual Response

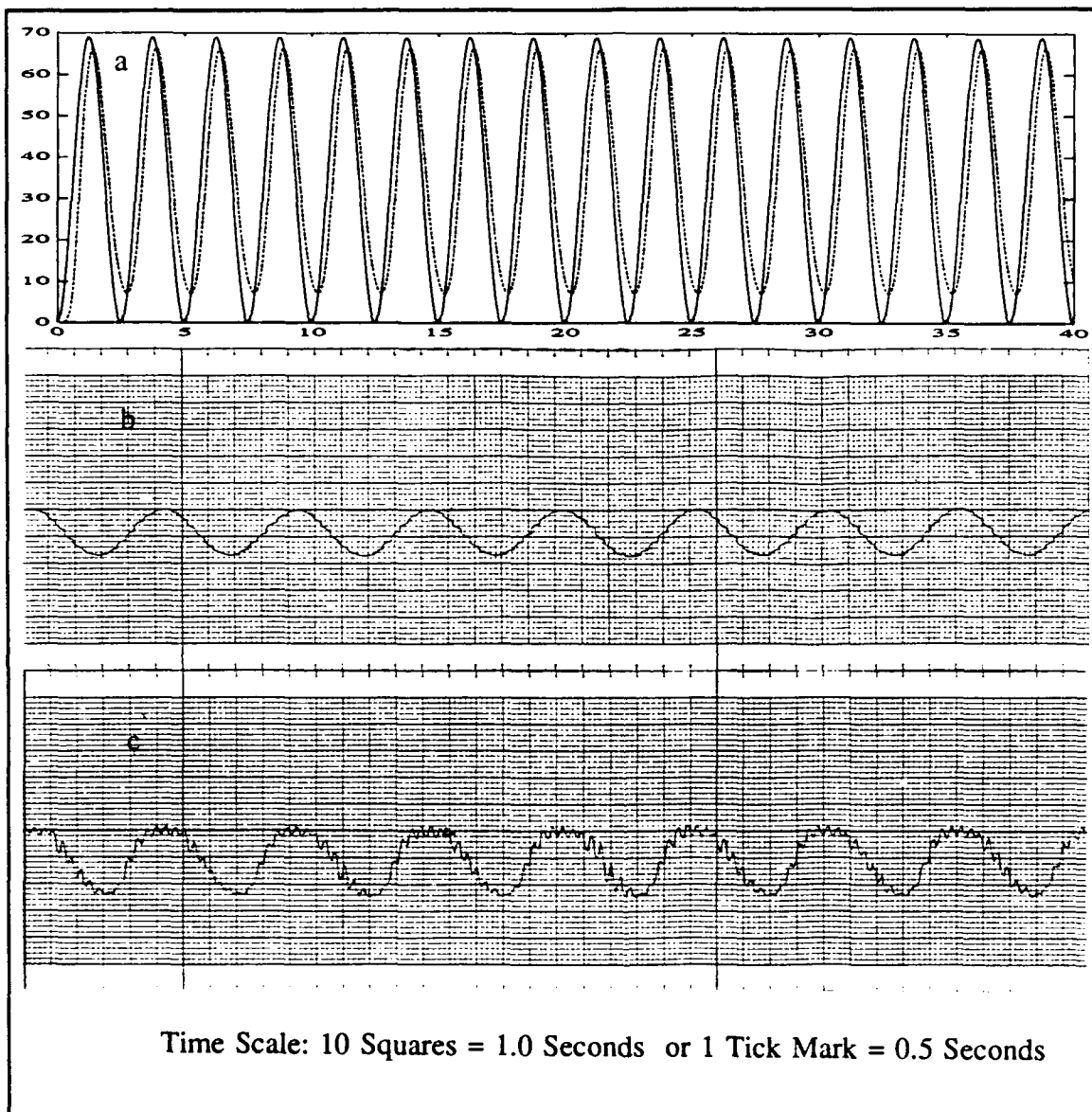


Figure 5.6 Sinusoidal Response, $T = 2.5$ Seconds, (a) Model Input and Response, (b) Actual Input, (c) Actual Response

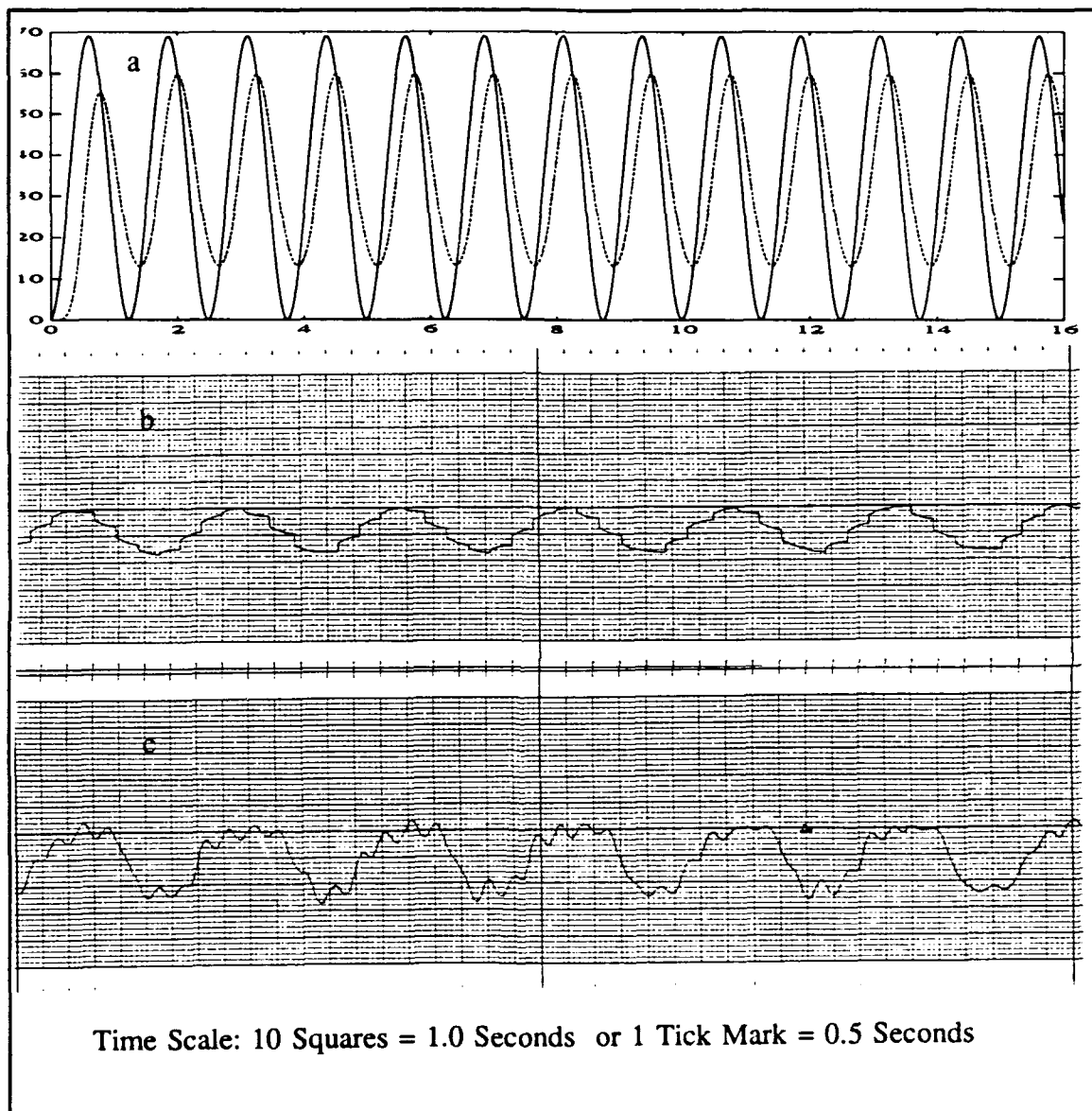


Figure 5.7 Sinusoidal Response, $T = 1.25$, (a) Model Input and Response, (b) Actual Input, (c) Actual Response

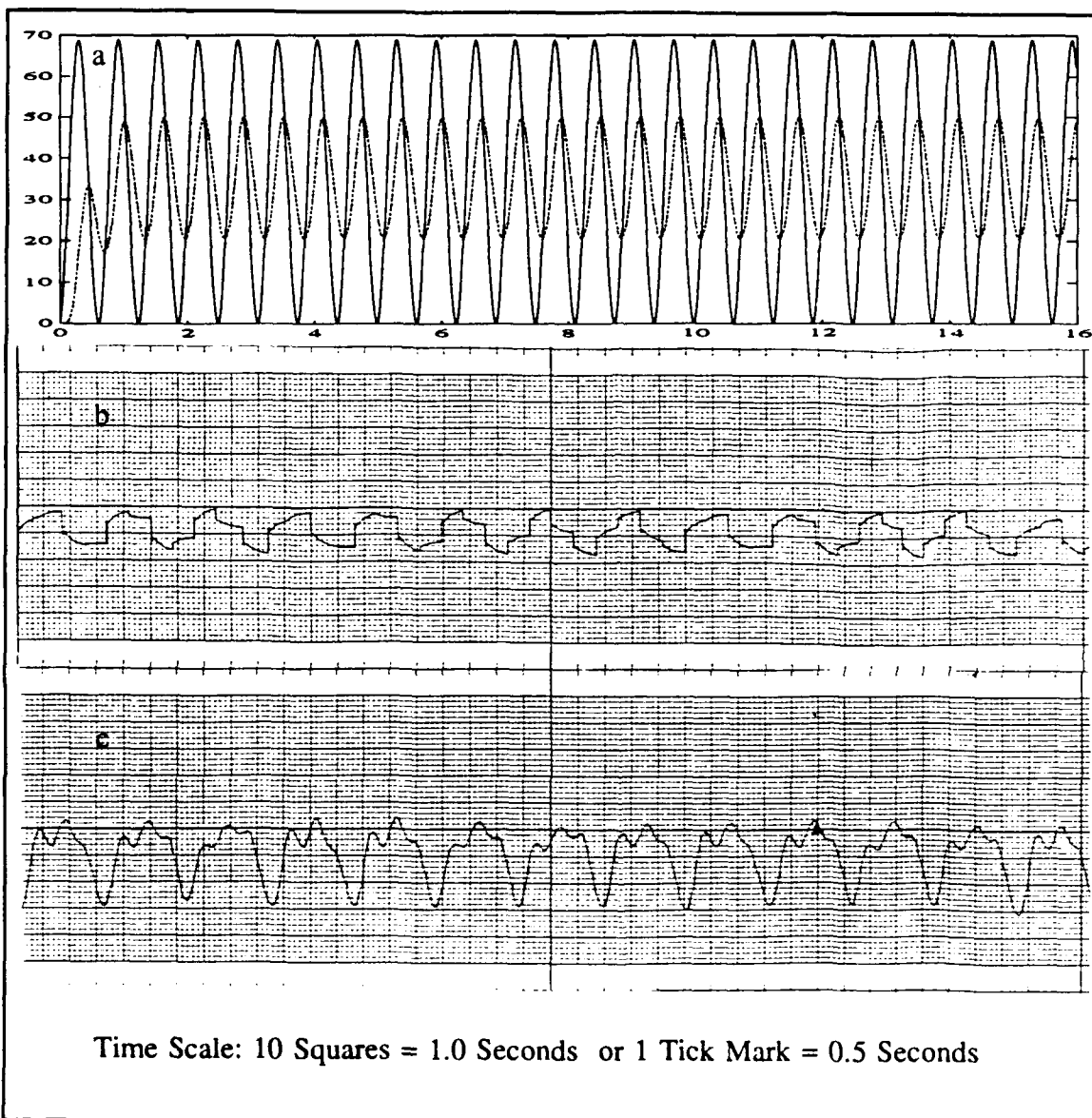


Figure 5.8 Sinusoidal Response $T=0.625$, (a) Model Input and Response, (b) Actual Input, (c) Actual Response.

By inspection of the sinusoidal responses, it is seen that the model accurately predicts the magnitude and the time lag of the actual thruster. This lag is firmly rooted in the hydrodynamics of the propeller. The time scale of this lag is the time necessary to develop the helical wake field downstream of the propeller after changes occur that effect the propeller's angular velocity. The model predicts the magnitude of this lag within 0.1 seconds of the actual response. The magnitude prediction is degraded for frequencies over 1 Hz where it under predicts the actual thrust developed by up to 40%.

5.4 Summary

The model developed in Chapter 4, and tuned in this chapter to match steady state and step responses, does a good job at predicting the dynamic response of the thruster. During the experimental studies, the actual thruster response is highly dependent on the adjustment of the controller to account for the inertia of the propeller. The controller used has two modes of operation: Torque control and Velocity control. The velocity control mode was very sensitive to the propeller inertia. If the controller is not well tuned, the velocity control mode becomes unstable. This risks damage to the mechanical linkages and uses a large amount of electrical power. Since this undesirable trait was not readily

correctable, all the comparisons use the controller's torque control mode. The model was tuned to best fit the controller when the controller was matched to the experimental propeller. In the next chapter, the model and controller were tuned to other motor and propeller combinations. The method of this chapter was used to tune all configurations tested.

Chapter 6

Steady State Performance Comparison of Several Thruster Units

6.1 Introduction

The purpose of this thesis is to design the best thruster unit for ABE. In order to verify the performance, the experimental thruster unit will be compared to other combinations of propellers and motor/gearbox units. In this chapter, four separate propellers and two motor/gearbox units are tested to determine steady state Power required to obtain a certain thrust at a bollard pull. The test setup described in Chapter 5 was used to gather the data. The results of these tests are compared to determine which thruster has the lowest power consumption over the desired range of thrust.

The motors/gearbox units under test were:

1. MFM Technology Inc. Series SM64 DC Brushless Motor with a 10:1 Gearbox.
2. Pittman elcom Series 5100 DC Brushless Motor with a 4:1 Gearbox.

The Propellers used in these tests were:

1. JASON Thruster Propeller; a 2-blade, 10-inch diameter propeller with a 4-inch pitch.
2. 18-inch diameter, 2-blade, model airplane propeller with a 6-inch pitch.
3. 18-inch diameter, 2-blade, model airplane propeller with an 8-inch pitch.
4. 18-inch diameter, 3-blade, Michigan Wheel Sailer Marine propeller with a 16-inch pitch.
(This is the EXPERIMENTAL Propeller)

Each combination of these components was tested in the two controller modes, Torque and Velocity control.

The "experimental" thruster consists of the MFM motor with the 10:1 gearbox and the Michigan Wheel propeller.

6.2 The ABE Thruster and Other Thruster Units

The thruster units will be categorized by the propeller used. The discussion starts with the smallest propeller and ends with the experimental propeller.

6.2.1 The JASON Propeller

The first propeller considered is the propeller from a JASON vehicle thruster. This propeller is used by the tethered underwater vehicle JASON and is equivalent to a standard 2-blade Mercury outboard motor propeller. Figure 6.1 shows the response of the JASON propeller to each motor/gearbox unit and controller mode. In this chapter the graph labels are decoded as follows:

The first letter indicates the motor unit under test, M corresponds to the MFM motor (10:1 reduction) and P corresponds to the Pittman Motor (4:1 reduction).

The middle 2 or 3 letters/numbers indicate the propeller used. JAS = the Jason Propeller, 86 = the 18" diameter 6" pitch airplane propeller, 88 = the 8" pitch airplane propeller, 316 = the Michigan Wheel 3-blade 16" pitch propeller.

The last letter indicates the controller mode, T = torque control, R = velocity control.

Examination of Figure 6.1 shows for the range of -10 to +10 lbf thrust, the Pittman motor/ 4:1 gearbox in torque mode outperforms the other methods of powering the JASON propeller.

For the 100 Watt ABE power budget limit, this unit provides a range of thrust from -8 lbf to +9 lbf at bollard.

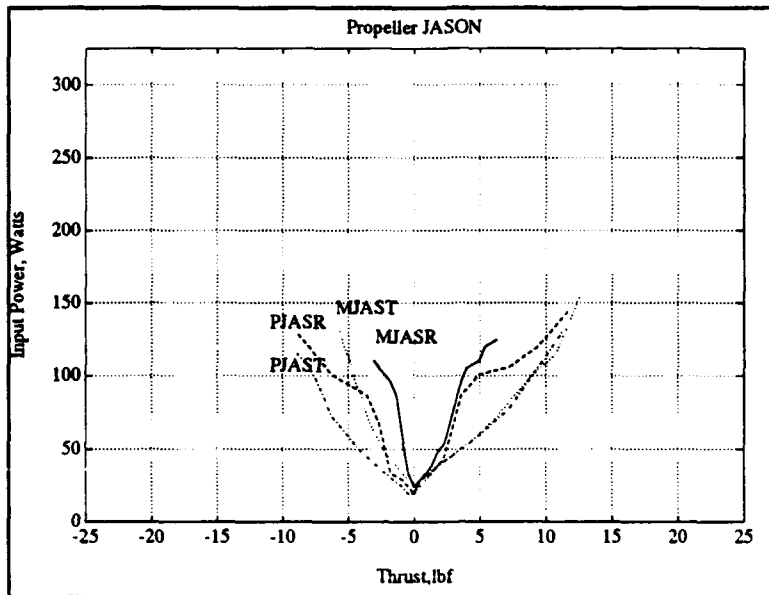


Figure 6.1 The Jason Propeller Response

6.2.2 The 86 Airplane Propeller

The second propeller is the 18-inch diameter model airplane propeller with a 6-inch pitch. This propeller is extremely asymmetric and is designed to be operated in only one direction. Figure 6.2 shows the steady state data for this propeller. Note the large difference in power required between forward and reverse thrust. For the +/- 10 lbf thrust range all thruster unit combinations are comparable, with the MFM motor in torque mode being the best. For ABE's 100 Watt limit, this propeller can provide -5 lbf to 12 lbf

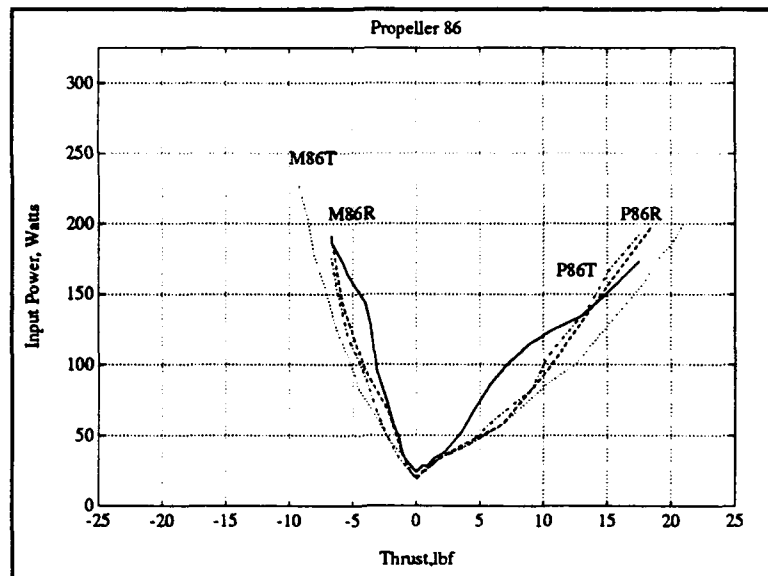


Figure 6.2 The 86 Airplane Propeller Response

6.2.3 The 88 Airplane Propeller

The 18-inch diameter model airplane propeller with an 8-inch pitch is very similar to the 86 propeller above. Figure 6.3 shows the data collected for this propeller. Again the MFM motor in torque mode outperforms the other combinations. The range of thrust available within the 100 Watt limit is -7 lbf to 13 lbf. This is slightly better than the 86 propeller performance.

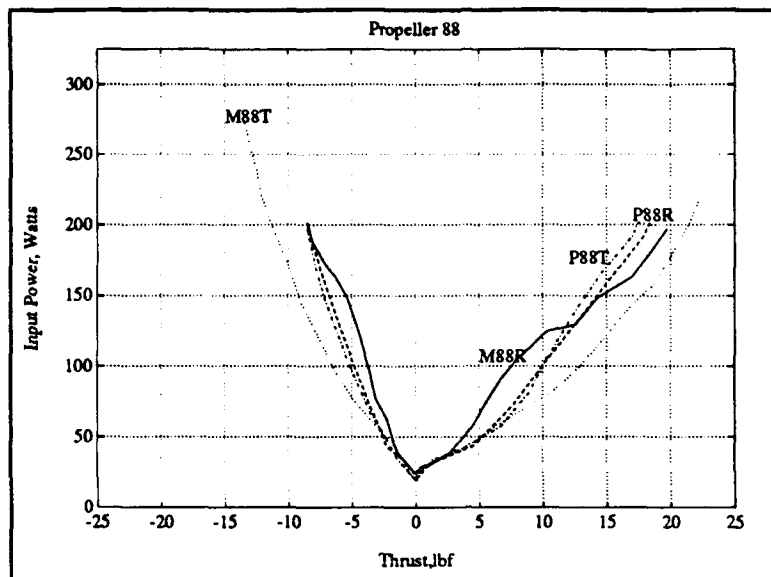


Figure 6.3 The 88 Airplane Propeller Response

6.2.4 The Experimental Propeller

The last propeller considered is the experimental propeller described in Chapter 2. This propeller, when matched with the designed motor/gearbox unit, outperforms the 4:1 gearbox in both controller modes. The range of thrust available under the 100 Watt limit is -7.5 lbf to 11 lbf. This propeller has the best bi-directional response of any of the tested propellers. Figure 6.4 shows the data for this propeller.

6.3 Steady State Comparison

Due to the limitation of the controller mentioned at the end of Chapter 5, the velocity control mode was not used for

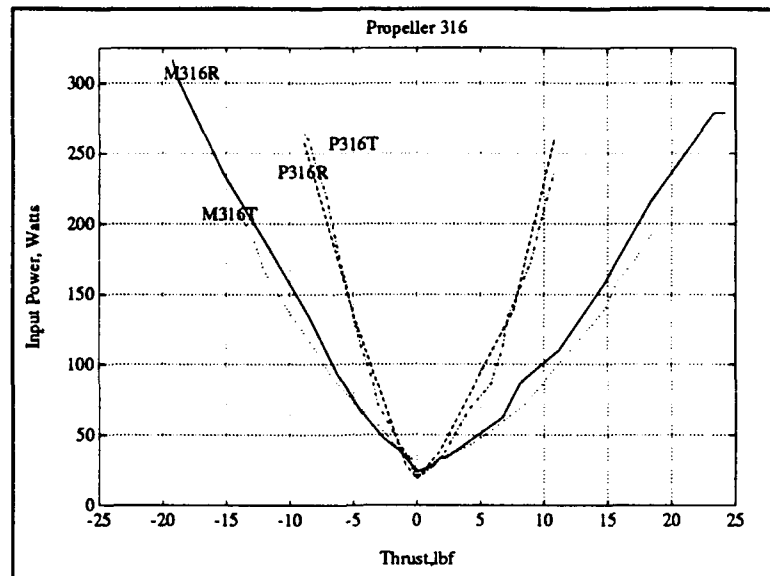


Figure 6.4 The Experimental Propeller Response

the final comparisons of the thruster units. The velocity mode shows a marked instability that is highly dependent on the inertia of the attached propeller. This instability causes an excess of power to be drawn at various speeds of operation, including stopped. Since the controller cannot be readily tuned to each propeller, the comparison of thruster units will be made with the data from the torque mode tests. Ideally, the steady state power consumption of the velocity mode can be tuned to a value close to the power used in the torque mode. The deficiency in this controller will be commented on in Chapter 8.

In general, the MFM motor with the 10:1 gearbox surpasses the Pittman motor with the 4:1 gear reduction. The only exception is the JASON propeller, which performed best with the Pittman motor unit. Since the motors are electrically

comparable, it can be inferred that the 10:1 gearbox is a better choice for the 88, 86 and 316 propellers.

The JASON propeller has the most limited range of thrust, regardless of power input. The maximum thrust for this propeller is near ± 10 lbf. This gives insufficient thrust for ABE's sprint capability of 2 knots (requiring about 13 lbf). Due to this limitation, the JASON Propeller will not be considered further.

Figure 6.5 shows the comparison of the propellers using the MFM motor in torque control and the 10:1 gearbox. For the forward thrust direction below 13 lbf, the 88, 86, and 316 propellers have nearly the same thrust/power characteristic. Since this is the region of interest, there is little to differentiate between the propellers. However, ABE will be operating in an area of current gradients. This means that forward and reverse thrusts will be necessary to maintain constant velocity while traveling on a closed circuit trajectory. Reverse thrust will also be necessary while ABE is maneuvering at docking. Therefore, the main propulsion thrusters should have the best possible reverse thrust efficiency without severely effecting the forward thrust characteristic. The 316 propeller has the lowest power consumption for any astern thrust demand. For comparison purposes, Figure 6.6 shows the velocity mode control curves for the MFM motor and all propellers. The tuning of the

controller increases the separation of the 316 curve from the other curves.

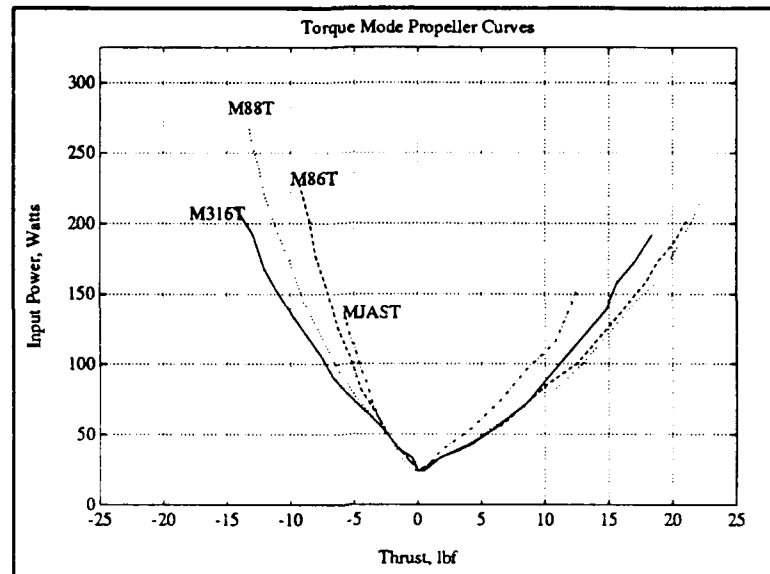


Figure 6.5 Propeller Comparison, Torque Mode, MFM Motor

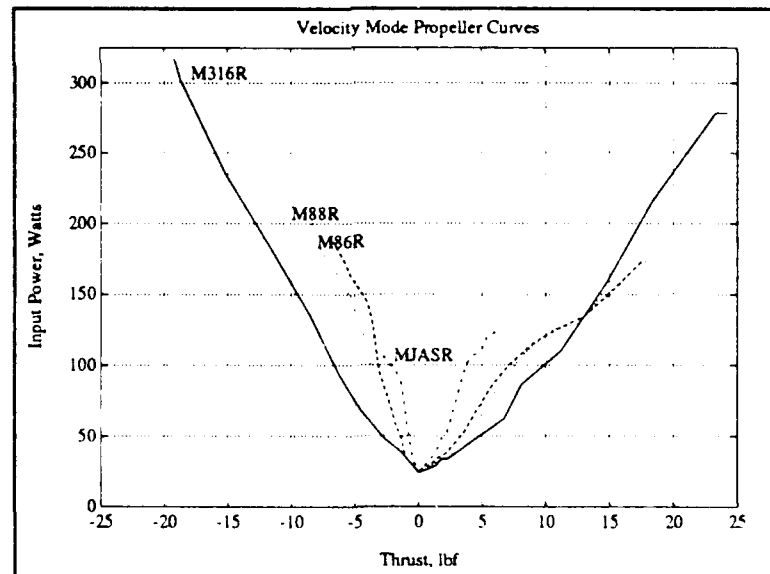


Figure 6.6 Propeller Comparison, Velocity Mode, MFM Motor

6.4 Summary

For steady state operation, the experimental thruster consumes less power than any other unit considered. In the range of - 10 lbf to + 10 lbf thrust demand, the experimental thruster has a power consumption advantage of 12% over the nearest competitor. This assumes that the thruster operates over a given trajectory, where any changes in thrust occur slowly and there is an equal demand of forward and astern thrusts. Chapter 7 examines the case where these assumptions are not valid.

Chapter 7

Balancing Dynamics and Efficiency

7.1 Introduction

Chapter 6 compared the combinations of propellers and motor/gearbox units in steady state. Although this gives important insight into the performance of the thrusters, this is only a small portion of the story. ABE will rarely operate in a "steady state" environment. During ABE's flight along a preprogrammed trajectory, there will be accelerations, constant velocity runs and unknown current gradients. These factors will drive ABE away from the steady state toward a richly dynamic environment.

In this chapter, the experimental propeller will be compared with the two model airplane propellers presented in Chapter 6. The experimental propeller will be driven by the MFM motor with the 10:1 gearbox. The airplane propellers will be combined with each of the two motor/gearbox units. The comparison will be based on the model of Chapter 4, with the parameters experimentally determined for each thruster. These parameters are shown in Table 7.1. The following definitions apply to Table 7.1:

Thruster 1 is the experimental thruster consisting of the MFM motor, the 10:1 gearbox, and the 316 propeller.

Thruster 2 is the MFM motor, the 10:1 gearbox, and the 88 propeller.

Thruster 3 is the same as thruster 2 except with the 86 propeller.

Thruster 4 and 5 are the same as 2 and 3 (respectively) except with the Pittman motor and the 4:1 gearbox.

Thruster	α	β	C_T
1 (M316)	0.10	23.0	0.0660
2 (M88)	0.18	27.0	0.0820
3 (M86)	0.09	20.0	0.0677
4 (P88)	0.33	2.85	0.4678
5 (P86)	0.23	2.85	0.4497

Table 7.1 Model Parameters

The response of each thruster was simulated on each of six trajectories: Hover, Track #1 through Track #5. The tracks (#1 through #5) are shown in Figure 7.1 . In the Hover mode, the simulated vehicle is initially displaced 1 centimeter off the desired position. The vehicle then attempts to regain and maintain the desired position.

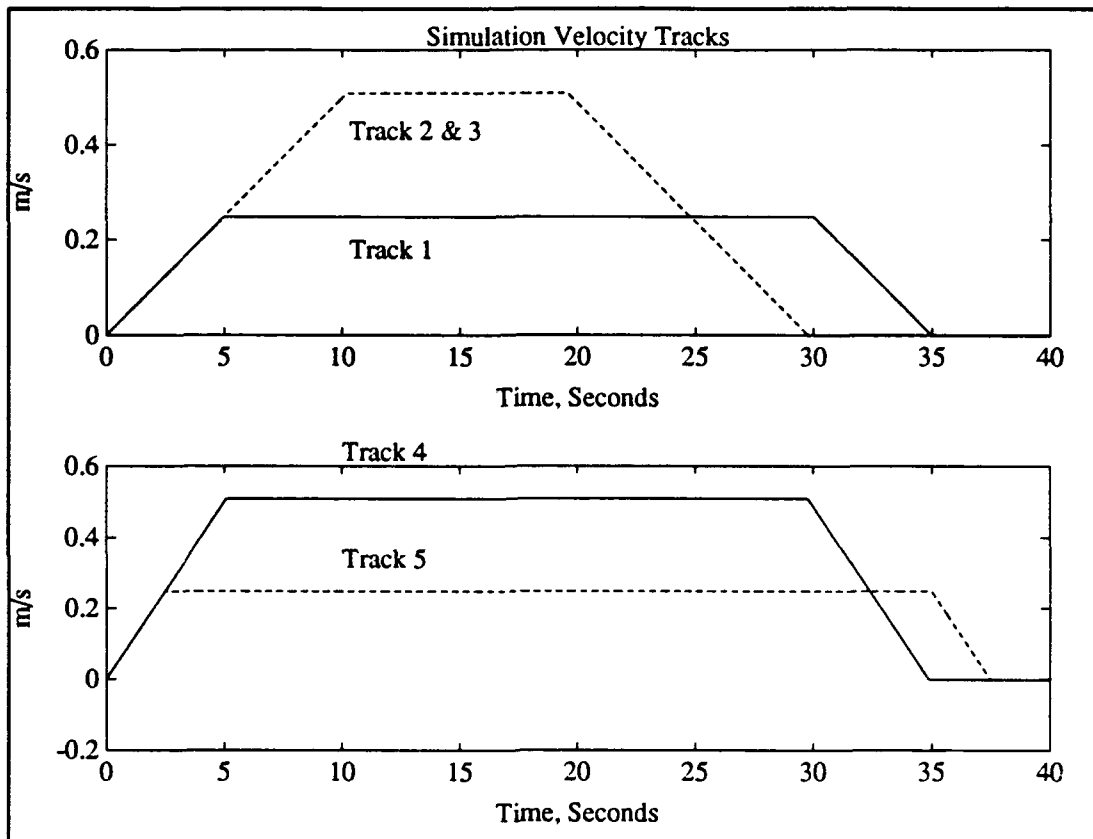


Figure 7.1 Tracks #1-5, Track 3 has a 0.5 m/s opposing current.

The qualitative description of the tracks is as follows:

- Track 1: **Low** Velocity, **Low** Acceleration, **No** Current.
- Track 2: **High** Velocity, **Low** Acceleration, **No** Current.
- Track 3: **High** Velocity, **Low** Acceleration, **Opposing**
Current.
- Track 4: **High** Velocity, **High** Acceleration, **No** Current.
- Track 5: **Low** Velocity, **High** Acceleration, **No** Current.

7.2 Dynamic Comparison

From step response data for each thruster unit under consideration, the speed of response can be rated. The criteria is the time until the thrust output stays within 5% of the final value. The thrusters were judged for a thrust step of 50 Newtons (approximately 11 lbf). The results are shown in Table 7.2

Thruster	Response Time
M88	0.55 sec
P88	0.60 sec
M86	0.60 sec
P86	0.65 sec
M316*	0.85 sec

Table 7.2 Time Response * Experimental Thruster

The 18-inch airplane propeller with an 8-inch pitch has the fastest response of all the propellers. For small thrust steps the differences between the speeds of response is large. For larger steps the time responses approach the same limit. The experimental propeller has the slowest response of the tested thrusters.

7.3 An Open Loop Force Controller

In order to evaluate the thrusters a simple force controller will be implemented. This will be a PD controller with poles placed such that the system's natural frequency is $\omega_n = 1.0$ rad/sec, and the damping ratio is $\eta = 0.707$.

7.3.1 The Simulated Vehicle

In order to test the thrusters on the aforementioned tracks, some vehicle dynamics must be considered. The vehicle modelled will be ABE. The drag of the vehicle is the drag calculated in Chapter 2. The drag at 1 knot is used to calculate an effective drag coefficient C'_D such that:

$$C'_D = \frac{1}{2} \rho A C_D = 190 \frac{kg}{m} \quad (7.1)$$

The effective mass of the vehicle will be the displacement of the three main body sections of ABE plus an added mass term. The added mass is used to account for the volume of water in and around the vehicle that must be accelerated in order for ABE to move through the water. For this analysis, the added mass is assumed to come from a sphere of water in front of each body section. Each sphere has a diameter equal to the maximum diameter of the associated section. The displacement of ABE is approximately 800 kg and

the added mass is about 160 kg. This leads to an effective mass of 960 kg.

Since three thrusters are used to drive the vehicle, and the point on their operating curves is significant to the analysis, it is assumed that the three thrusters share the load equally at all times. This allows the simulation to be run for one thruster using one third of the values calculated above. Therefore each thruster will 'see' an effective drag coefficient of $C'_D = 22.67 \text{ kg/m}$ and an effective mass of 320 kg.

7.3.2 Power Consumption Comparison

Each thruster was run on each simulated track. The average power during the run was computed and tabulated in Table 7.3. Initially, it is assumed that the thruster has the same forward and reverse power to thrust characteristic. Double line blocks indicate the lowest mean power consumption for a particular trajectory.

Thruster	Hover	Track #1	Track #2	Track #3	Track #4	Track #5
1 (M316)	19.96	24.56	29.30	39.86	34.59	27.65
2 (M88)	19.47	24.53	29.96	41.56	35.61	27.24
3 (M86)	20.19	24.72	29.42	39.99	34.73	28.45
4 (P88)	19.85	26.26	33.17	47.98	40.50	30.16
5 (P86)	20.26	25.00	29.92	40.99	35.49	28.96

Table 7.3 Mean Power Consumption in Watts

The assumption of equal ahead and astern performance is not valid (see Chapter 6, Figure 6.5). A penalty factor must be applied to each thruster to correct for the increased power consumption in the astern thrust direction. The penalty factor (PF) used in this analysis is the ratio of slopes from the steady state power versus thrust characteristic for each thruster (Figure 6.5). The penalty factor for each thruster is shown in Table 7.4 . In order to apply this correction, some assumption must be made about the ratio of time at ahead thrust versus the time at astern thrust. When it is assumed that the thruster operates between 1/4 and 1/2 of the time astern, the results for Tracks #1,2,4,and 5 are the same in terms of thruster ranking. (ie. the sensitivity to this

assumption is low) Except as specifically noted, it is assumed for a given track, that one third of the time is spent under astern thrust conditions. It is further assumed that the astern thrust distribution is the same as the ahead thrust distribution. Track 3 and Hover mode are the exceptions. Since Track 3 has a constant opposing current, it is assumed that the thruster only operates in the ahead direction. For the Hover mode, it is assumed that the thruster operates for equal times at ahead and astern thrust.

In addition to the correction for the asymmetric nature of the propellers, the quiescent power load (PQ) of the controller must be removed. This load is the power the controller draws in spite of the load from the motor operation. For the controller used in these tests, this load is $PQ = 19.2$ watts. This 19.2 Watts is high and obscures the effect of the propellers. The equation used to apply both corrections is:

$$\bar{P}_{corr} = \frac{2}{3} (\bar{P} - PQ) + \frac{1}{3} (\bar{P} - PQ) PF \quad (7.2)$$

Thruster	Penalty Factor
1 (M316)	1.91
2 (M88)	2.13
3 (M86)	2.89
4 (P88)	2.62
5 (P86)	3.03

Table 7.4 Penalty Factors

In order to evaluate the power used by the propeller and controller to accelerate the vehicle mass, it is helpful to remove the portion of the mean power used to overcome the vehicle drag. This mean power is calculated by integrating (Drag Force)*(Velocity) for each track, and then dividing by the simulation duration. The resulting mean power data after correcting for asymmetry, and removing the quiescent and 'drag' power, is shown in Table 7.5. The last row of this table is the calculated mean power required to overcome the drag for each track. Double boxes indicate the lowest mean power for a given track.

Thrust er	Hover	Track #1	Track #2	Track #3	Track #4	Track #5
1	1.11	6.70	11.91	6.90	17.77	10.66
2	0.40	7.05	13.56	8.60	20.30	10.72
3	1.93	8.71	15.41	7.03	33.02	14.73
4	1.17	10.58	20.26	15.02	30.51	16.53
5	2.14	9.43	16.72	8.03	25.02	16.01
'Drag' Power	0.00	0.29	1.25	13.76	2.29	0.35

Table 7.5 Corrected Mean Power Data in Watts

Table 7.3 shows that the 88 propeller is tied for first place with the 316 propeller. When the 88 propeller is corrected, its loss of efficiency in reverse thrust operation drops this propeller to second place. This conclusion holds for several correction formula weights between $1/4$ and $1/2$. All the weights calculated gave results similar to those presented in Table 7.5.

Figure 7.2 shows a break down of mean power consumption for each track and thrusters 1,2 and 3. The cross-hatched section up to 19.2 Watts indicate the controller's quiescent power load. The solid filled region immediately above the 19.2 level indicates the power required on each track to

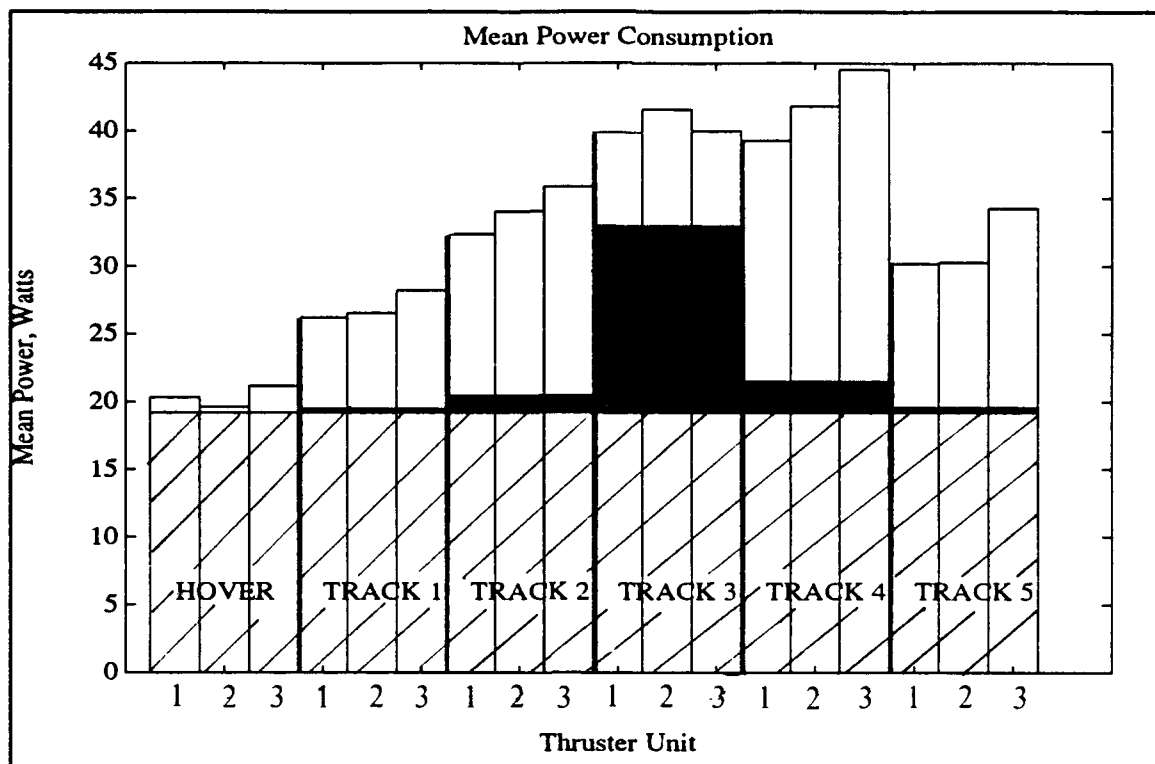


Figure 7.2 Power Consumption

overcome vehicle drag. The enclosed area remaining above this level accounts for the remaining power used by the controller and the propeller to accelerate the vehicle and overcome the hydrodynamic losses.

7.3.3 Comparing the Dynamics

The 316 propeller has the best power consumption over the tracks tested, with the exception of Hover. The Track 2 velocity response of the 316 propeller is shown in Figure 7.3. Figure 7.4 shows the same response for the 88 propeller.

The position response for both propellers in Hover mode is shown in Figure 7.5 .

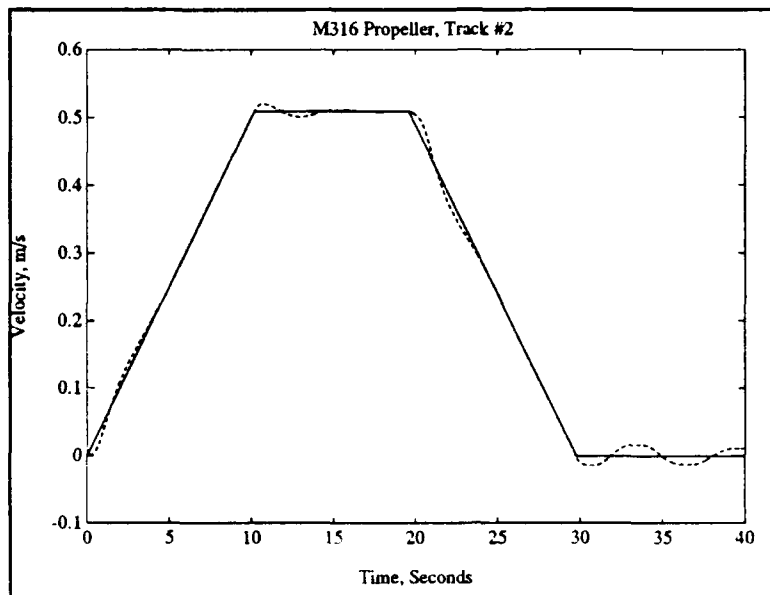


Figure 7.3 Experimental Thruster Track #2, Velocity Response

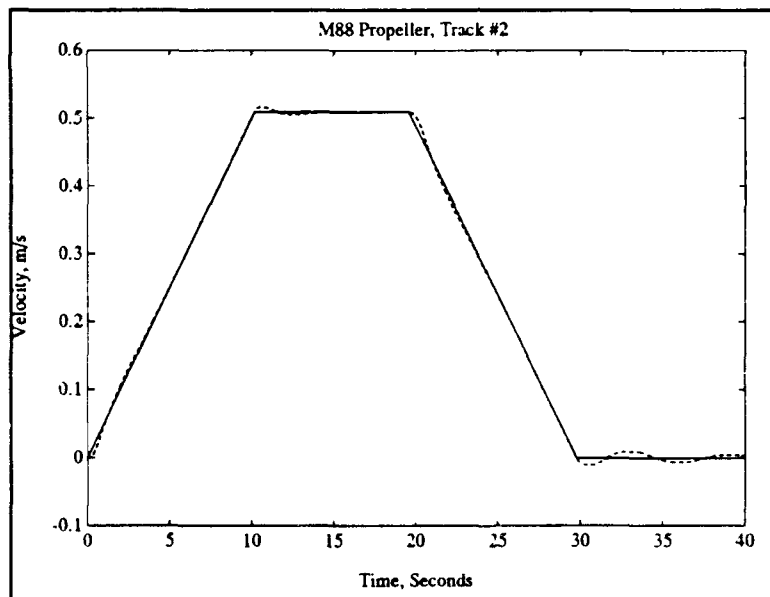


Figure 7.4 The M88 Thruster, Track #2, Velocity Response

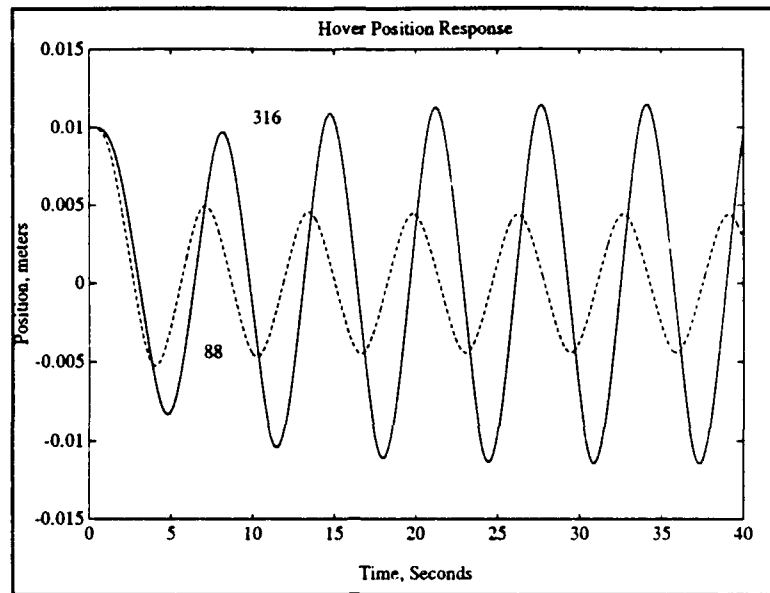


Figure 7.5 Thruster Hover Response

7.4 Summary

The simulations presented in this chapter show there is a trade-off between power conservation and rapid dynamic response. This is clearly illustrated by the data for the Track 2 simulations presented in Table 7.5, Figures 7.3 and 7.4. The M88 thruster follows the velocity track better than the M316 thruster. The cost of this slightly improved response is 2 Watts, a 14% increase over the mean power consumed by the M316 thruster. This 2 watts, when multiplied by three forward propulsion thrusters, is 6% of the total propulsion budget for ABE.

Better dynamics is a more important criteria when evaluating the hover mode thrusters. By responding quickly,

the M88 thruster reduces the magnitude of the hover limit cycle. This in turn limits the vehicle velocity and power is saved. This is shown by the plot in Figure .5, where the M88 thruster uses 40% of the power used by the M316 thruster.

For a typical ABE track having long constant velocity legs, rapid dynamics are less important. For a well developed controller, providing slow acceleration up to survey speed, the M316 thruster is the optimum choice. The cost in dynamic response is negligible in this case and the power savings is significant (14% for Tracks 2 and 4).

Chapter 8

Summary, Conclusions, and Recommendations

The purpose of this thesis was to develop an optimized propulsion system for ABE. From the beginning, special attention was given to maximizing the power efficiency of the system's components. In this light, a propeller was designed specifically for the ABE vehicle and its predicted mission profile. This custom propeller was then matched to a suitable DC brushless motor. These units were connected via a speed reducing gearbox, thus taking advantage of the high efficiency operating regions of both components.

Following its design, the ABE thruster was modelled using non-linear lumped parameter modelling techniques. The final model was reduced to three parameters (C_T , α , β) describing the thruster. Using this model, five different thrusters were evaluated, including the designed ABE thruster. The three parameters for each thruster were determined experimentally, using system identification methods. From the experimental data and the modelled response, the static and dynamic performance of the thrusters was compared. Finally, a simple controller was implemented, and a simulated ABE vehicle with

model thrusters, was run on several tracks. This allowed evaluation of the control performance of each thruster.

The result of this analysis indicates there is a trade-off between control performance and efficiency. In general, the designed propeller had the highest efficiency and the slowest response. The propeller with the fastest response, demanded more power in order to achieve this improved performance. The exception is in hover mode where the improved response limited the vehicle limit cycle and resulted in power savings. The simulated trajectories were typical of the predicted ABE track profiles. From these simulations, it became evident that the power used to overcome hydrodynamic drag is nearly insignificant for the proposed ABE operating velocities. The overwhelming share of the power goes first, to powering the control electronics, then to the un-modelled hydrodynamics and the power required to accelerate the vehicle's mass. Therefore, the use of the typical drag calculation is not sufficient to predict the propulsive power requirements for ABE.

As the track length increases from the simulated track length, which is on the order of 10 meters, the importance of improved propeller dynamics is overshadowed by the need for higher efficiency. For ABE, this means that the designed high efficiency propeller is the best choice. The power cost for the improved propeller response is too high (6-14% as modelled) and the improvement in velocity tracking is small.

Additionally, the limitations imposed by the slower response of the designed thruster can be compensated for by the intelligent application of control algorithms. Further research should start by determining the best way to control the thruster in order to best exploit its improved efficiency and to correct for the slow response. Following closely behind additional control research, should be the coordinated planning of the ABE trajectories. These tracks must be developed in a manner that allows the control system to operate the thrusters at peak efficiency. This includes using low accelerations and maximizing constant velocity legs as much as possible. Simulation runs with rapid acceleration to speed, consumed up to 60% more power than low accelerations to the same velocity.

References

- [1] Yoerger, D.R. et al.; "The Autonomous Benthic Explorer (ABE): A Deep Ocean AUV for Scientific Seafloor Survey."; WHOI #7569; Woods Hole Oceanographic Institution; Sept. 1990.
- [2] Kerwin, J.E.; Hydrofoils and Propellers, 13.04 Lecture Notes; MIT; January 1991.
- [3] Newman, J.N.; Marine Hydrodynamics; MIT Press; Cambridge, Massachusetts; 1977.
- [4] Abbott, I.H., Von Doenhoff, A.E.; Theory of Wing Sections; Dover Publications, Inc.; New York; 1949.
- [5] Pittman elcom® Brushless D-C Servomotors, Bulletin 5000, Technical Data Sheet, March 1989.
- [6] Bradley, A.; Woods Hole Oceanographic Institution Internal Memo; Motor & Gearbox Studies; Fall 1990.

- [7] Cooke, J.G.; "Incorporating Thruster Dynamics in the Control of an Underwater Vehicle"; Engineers Degree Thesis, MIT/WHOI Joint Program in Oceanographic Engineering; Woods Hole, Massachusetts; Sept. 1989.

- [8] Abkowitz, M.A.; Stability and Motion Control of Ocean Vehicles; The MIT Press; Cambridge, Massachusetts; 1969.

- [9] Currie, I.G.; Fundamental Mechanics of Fluids; McGraw-Hill, Inc; New York; 1974.

- [10] Beaman, J.J., Breedveld, P.C.; "Physical Modeling with Eulerian Frames and Bond Graphs"; Transactions of the ASME; Vol. 110; June 1988; Pages 182-188.

- [11] Ogata, K.; Modern Control Engineering; Prentice-Hall, Inc.; New Jersey; 1970.

- [12] Yoerger, D.R. et al.; "The Influence of Thruster Dynamics on Underwater Vehicle Behavior and Their Incorporation Into Control System Design"; IEEE Journal of Oceanic Engineering; Vol. 15; No. 3; July 1990.